Geochemical evidence from the Kioto Carbonate Platform (Tibet) reveals enhanced terrigenous input and deoxygenation during the early Toarcian

Zhong Han[1, 2], Xiumian Hu[2]*, Zhongya Hu[3], Hugh C. Jenkyns[4], Tianhao Su[5]

1 Key Laboratory of Deep-time Geography and Environment Reconstruction and Applications, MNR & Institute of Sedimentary Geology, Chengdu University of Technology, Chengdu 610059, China

2 State Key Laboratory of Mineral Deposit Research, School of Earth Sciences and Engineering, Nanjing University, Nanjing 210023

3 State Key Laboratory of Marine Geology, School of Ocean and Earth Science, Tongji University, Shanghai, China

4 Department of Earth Sciences, University of Oxford, South Parks Road, Oxford OX1 3AN, UK

5 College of Earth Sciences, Chengdu University of Technology, Chengdu 610059, China

**Corresponding author: Dr. Xiumian Hu*

E-mail: huxm@nju.edu.cn; Tel: 0086 25 89683002

ABSTRACT

The early Toarcian, as registered in a variety of sedimentary archives, was characterized by an abrupt negative carbon-isotope excursion (CIE) typically superimposed on a long-term positive trend, and was accompanied by significant climatic

and environmental changes. However, the changes in continental weathering influx and oceanic deoxygenation in shallow waters and their possible role in causing carbonate-platform crises in low latitudes remains poorly constrained. Here, we present carbonate content and carbonate-hosted elements for the Pliensbachian–Toarcian transitional interval from the Kioto Carbonate Platform (KCP) in the Tibetan Himalaya. The most water-insoluble elements (e.g. Ti, Sc, Th and total rare earth elements) show an obvious increase starting at the Pliensbachian–Toarcian boundary, followed by a weak increase or relatively high-level values during the negative phase of the T-OAE CIE, suggesting that the enhanced terrigenous input can be linked to rapid global warming during this time interval. The Mn, Ce and Ce anomaly start to increase immediately following the rise in abundance of the water-insoluble elements, followed in turn by enhanced values over the interval of the negative CIE. These observations indicate that the deoxygenation process and development of manganous (suboxic) conditions occurred in shallow water during this time interval and were likely linked to enhanced continental weathering and nutrient input, favoring both primary productivity and oxygen consumption. Stratigraphically higher, the water-insoluble elements show a gradual decreasing trend parallel with elevated values of redox proxies during the recovery phase of the CIE, suggesting decline in continental weathering intensity and a corresponding second deoxygenation in shallow waters. In this instance, deoxygenation might have been caused by a slackening of ocean circulation and/or enhanced recycling of bioessential nutrients. The coupled relationship between biotic changes, carbonate content and geochemical data suggest that: (1) the onset of enhanced terrigenous influx and deoxygenation in shallow waters likely led to slight deterioration to the KCP around Pliensbachian–Toarcian boundary time, and (2) the

drastically enhanced terrigenous flux and deoxygenation likely played a pivotal role in the more severe crisis for benthic carbonate producers during the negative phase of the CIE.

Keywords: Toarcian OAE; Carbonate platform; Major and trace elements; Enhanced terrigenous input; Deoxygenation; Tibetan Himalaya

1. Introduction

The early Toarcian (~183 Ma) witnessed one of the most widely recognized Oceanic Anoxic Events (OAEs) owing to the widespread expansion of oxygen-depleted waters and global distribution of coeval organic-rich sediments from both epicontinental and pelagic settings (T-OAE; Jenkyns, 1988, 2010). This interval of geological time was characterized by major climatic and environmental perturbations such as rapid global warming (e.g. Bailey et al., 2003; Suan et al., 2010; Dera et al., 2011; Ruebsam et al., 2020; Jenkyns and Macfarlane, 2022), enhanced continental weathering (e.g. Percival et al., 2016; Brazier et al., 2015; Kemp et al., 2020), significant sea-level rise (e.g. Hallam, 1981; Hesselbo and Jenkyns 1998; Han et al., 2016; Ruebsam et al., 2019), ocean acidification (e.g. Trecalli et al., 2012; Ettinger et al., 2020; Müller et al., 2020), and a biotic crisis (e.g. Harries and Little, 1999; Caruthers et al., 2014; Caswell et al., 2014; Jiang et al., 2020). These changes were closely linked to significant carbon-cycle disturbance characterized by an abrupt negative carbon-isotope excursion (CIE) interrupting a long-term positive CIE (Jenkyns and Clayton, 1997; Hermoso et al., 2009a; Jenkyns et al., 2010; Xu et al., 2018; Storm et al., 2020). The T-OAE CIE has been variously linked to rapid, large-scale CO_2 release from the Karoo–Ferrar Large Igneous Province, dissociation of methane hydrate in continental

54 margins and/or terrigenous environments of wetlands, lakes and soils (e.g. Pálfy and Smith,
55 2000; Hesselbo et al., 2000; Them et al., 2017a).

56 During OAEs, enhanced continental silicate weathering consumes the inorganic
57 carbon directly and increases nutrient supply to the oceans. Consequent effects include
58 expansion of oxygen-depleted waters with increased productivity of marine organic matter
59 and its subsequent burial in the ocean: phenomena that could have played a central role in
60 drawdown of excess atmospheric CO_2 (Jenkyns, 1988, 2010 and references therein).
61 Although these two environmental changes have been widely recognized by multiple
62 isotope systems (e.g. calcium, molybdenum, nitrogen, osmium, strontium, sulfur and
63 thallium) during the T-OAE (e.g. McArthur et al., 2000; Jenkyns et al., 2001; Cohen et al.,
64 2004; Gill et al., 2011; Newton et al., 2011; Brazier et al., 2015; Percival et al., 2016;
65 Dickson et al., 2017; Them et al., 2018; Kemp et al., 2020), the vast majority of the
66 investigated sections are from the northern hemisphere, especially northern and southern
67 Europe. To date, only sparse low-resolution $\delta^{34}S$ data from carbonate-associated sulfate
68 derive from Tibet, originally positioned in the southern hemisphere, additionally suggest a
69 globally distributed oceanic oxygenation deficiency (Newton et al., 2011; Han et al., 2022).
70 However, the sulfur-isotope data have been considered as a potentially modified signal due
71 to the much larger magnitude $\delta^{34}S$ values relative to those in coeval sediments from Europe
72 (Gill et al., 2011). The northern hemisphere bias thus limits our understanding of the
73 feedback mechanisms responding to massive carbon injection into the ocean–atmosphere
74 system in a comprehensive global context.

75 Notably, shallow-water carbonate platforms were widespread in the tropics/subtropics
76 along the southern Tethyan margins during the Early Jurassic, where biologically diverse

77 shallow-water ecosystems were located (e.g. Woodfine et al., 2008; Bodin et al., 2010;
78 Trecalli et al., 2012; Han et al., 2016, 2021; Ettinger et al., 2020; Jenkyns, 2020). These
79 biotic carbonate platforms were commonly modified by drowning or a shift to non-skeletal
80 carbonates during the early Toarcian, temporally consistent with the extinction of reef-
81 building *Lithiotis* bivalves as well as other benthic organisms (Trecalli et al., 2012;
82 Sabatino et al., 2013; Han et al., 2018; Jiang et al., 2020; Krencker et al., 2020). Drowning
83 and foundering of these Tethyan carbonate platforms was the ultimate response of these
84 shallow-marine ecosystems to significant global palaeoenvironmental and
85 palaeoceanographic perturbation. Among the possible detrimental environmental changes,
86 enhanced terrigenous input and oxygen depletion are commonly believed to be the two
87 main factors that are disadvantageous to benthic communities and shallow-water carbonate
88 production in geological history (Föllmi et al., 2006; Godet, 2013; Krencker et al., 2020;
89 Reijmer, 2021). However, there is a paucity of effective geochemical proxies from shallow-
90 water carbonate platforms that can directly capture information regarding regional and/or
91 global changes in terrigenous input and oxygen availability (cf. Trecalli et al., 2012; Han
92 et al., 2018; Krencker et al., 2020).

93 From the lower Toarcian of the High Atlas Platforms in Morocco, pulses of
94 terrigenous input have been recognized that could have been a major control behind the
95 shutdown of this carbonate factory (Wilmsen and Neuweiler, 2008; Bodin et al., 2010;
96 Krencker et al., 2020). However, such a mechanism is unlikely in other sites, particularly
97 in the case of the relatively isolated Campania–Lucania and Adriatic Platforms (Trecalli et
98 al., 2012; Sabatino et al., 2013; Ettinger et al., 2020). However, studies do exist of redox
99 conditions by carbonate-hosted I/Ca, Mn/Ca and Ce anomalies (Ce/Ce*) from the

Campania–Lucania Platform, Italy and Mn from the Adriatic Platform, Croatia (Lu et al., 2010; Sabatino et al., 2013), and by bulk-rock hosted Fe, V, Ni and Mo from the Adriatic Platform, Slovenia (Ettinger et al., 2020). These redox proxies suggest a drawdown of oxygen content in the shallow tropical waters, although extreme oxygen depletion is inconsistent with sedimentological evidence of "spotted limestones", characterized by high bioturbation density, in Croatia and reddish oxidized claystones in Morocco within the T-OAE interval (Sabatino et al., 2013; Krencker et al., 2015). Therefore, the exact role of enhanced continental weathering and anoxia in fostering a neritic carbonate crisis remains controversial.

In the Southern Hemisphere, the Tibetan Nianduo section from the shallow-water Kioto Carbonate Platform has been well studied for foraminiferal biostratigraphy, sedimentology and carbon-isotope stratigraphy, enabling recognition of the typical T-OAE CIE (Han et al., 2016, 2018; Jiang et al., 2020). Here, we present $CaCO_3$ content, major and trace elements of shallow-marine carbonate from the Pliensbachian–Toarcian transitional interval of the Nianduo section in order to constrain changes in continental weathering and ocean deoxygentaion in shallow tropical waters in the eastern Tethys of the Souhern Hemisphere. The data obtained in this study are then integrated with those from the western Tethyan continental margin and European shelf to assess the extent of global changes potentially affecting carbonate platforms during this time interval at supra-regional Tethyan scale.

2. Geological setting and stratigraphy

The study area is located in the Tethys Himalaya of southern Tibet, which represents the northern margin remnants of the Indian continent and is now tectonically separated by

123 the Yarlung Zangbo Suture Zone in the north and the Greater Himalaya in the south (Fig.
124 1; Sciunnach and Garzanti, 2012). During the Jurassic, the Tethys Himalaya was located in
125 near-equatorial zones of the Southern Hemisphere directly facing the southeastern
126 Neotethys Ocean. The Kioto Carbonate Platform (KCP) developed along the southern part
127 of the Tethys Himalaya in the Early Jurassic (Jadoul et al., 1998; Sciunnach and Garzanti,
128 2012; Han et al., 2021).

129 The KCP has been well studied in the Nianduo (Fig. 2A) and Wölong sections of
130 southern Tibet, the carbonate deposits of which are closely comparable and have been
131 subdivided into the Pupuga and Nieniexiongla Formations (Jadoul et al., 1998; Han et al.,
132 2016; 2018; 2021). The Pupuga Formation was deposited on a shallow-water carbonate
133 platform and is characterized by thick-bedded bioclastic packstones/grainstones (Fig. 2B),
134 whereas the overlying Nieniexiongla Formation was formed on a deeper-water carbonate
135 ramp whose lower part is dominated by thin-bedded micrites (Fig. 2C) alternating with
136 common coarser-grained tempestites and whose upper part is characterized by more
137 abundant terrigenous siltstones (Jadoul et al., 1998; Han et al., 2016; 2018; 2021). The
138 Pupuga Formation spans the Pliensbachian to lowest Toarcian interval based on the
139 biostratigraphical data of larger benthic foraminifera and *Lithiotis* bivalves (Han et al.,
140 2018, 2021). The lower Nieniexiongla Formation is roughly dated as Toarcian to Aalenian
141 inferred from the Toarcian foraminifera in the basal units and a Bajocian ammonite in the
142 upper part (Jadoul et al., 1998; Han et al., 2021). On the basis of biostratigraphy, the
143 Pupuga–Nieniexiongla transitional interval records the typical characteristics of the T-OAE,
144 such as evidence for rapid sea-level rise and biotic carbonate-platform crisis, the presence
145 of abundant tempestite layers and characteristic T-OAE CIE and accompanying positive

146 sulfur-isotope excursion (Newton et al., 2011; Han et al., 2018, 2021, 2022). Additionally,
147 the small negative CIE (~ −12 to −5 m) in $\delta^{13}C_{TOC}$ recorded in the Nianduo section has
148 been assigned to the Pliensbachian–Toarcian boundary based on foraminiferal
149 biostratigraphy (Han et al., 2018, 2021; Jiang et al., 2020).

150 **3. Materials and methods**

151 *3.1 Sample selection*

152 Samples were collected from the transitional interval of the Pupuga–Nieniexiongla
153 Formations of the Nianduo section in the southern part of the Tethys Himalaya that records
154 the T-OAE (Fig. 2A; Han et al., 2018). Notably, common storm-generated beds with visible
155 terrigenous content under the microscope (e.g. fine-grained quartz and a little clay) occur
156 in the lower part of the T-OAE CIE interval, which could potentially contaminate the
157 leaching procedure using acetic acid (HAC) (see section 3.2). Thin-sections of these
158 samples therefore were firstly checked to select the best-preserved rock components ('pure'
159 carbonate in this study) lacking storm-originated terrigenous grains and without evidence
160 of recrystallization and metamorphism. Finally, the selected samples from the Pupuga
161 Formation (below 0 m) are characterized by grainstones with minor
162 packstone/wackestones (Fig. 2D-G), and from the Nieniexiongla Formation (above 0 m)
163 are dominated by mudstone (Fig. 2H-I) with storm-generated coarser
164 packstone/wackestone (Han et al., 2016, 2018). These samples were cut into fresh rock
165 chips that were then micro-drilled to produce powder, taking care to avoid cement-filled
166 pores, veins and bioclasts.

167 *3.2 Calcium carbonate content and elemental concentration*

168 70 samples in total were selected to perform the analysis of calcium carbonate content

using a NFP18-508 pressure calcimeter at the State Key Laboratory of Marine Geology of Tongji University, China. This instrument determines the $CaCO_3$ content (wt.%) based on the partial pressure of resultant CO_2 from reaction of $CaCO_3$ and HCl. Approximately 100 mg carbonate power of each bulk sample was dissolved in excess 10% HCl and the produced CO_2 volume was then used to calculate the $CaCO_3$ content. Pure carbonate standards and replicates were performed every ten samples to control the uncertainty. A long-term instrument error of this method is less than 2%.

We selected 67 bulk carbonate samples in the key interval from the Pliensbachian–Toarcian boundary to the T-OAE CIE interval for element analyses, which largely but not completely correspond with samples used for $CaCO_3$ content. About 50 mg powder of each carbonate sample was weighed and subsequently dissolved in 5 mL 10% acetic acid. After 12 h, 0.5 mL solution of each sample was transferred into a new pre-cleaned Teflon beaker, and then the aliquot was repeatedly dried with 1 mL concentrated HNO_3 three times to transform the dissolved samples into nitrate. The samples were finally diluted in 15 mL 2% HNO_3. We performed the element analyses using an Agilent 7900 ICP-MS also at the State Key Laboratory of Marine Geology at Tongji University. The analytical precision was better than 5% (RSD) for all selected elements.

3.3 Cerium anomaly

The cerium anomaly (Ce/Ce*) is calculated based on the relative depletion or enrichment in PAAS- (Post-Archean Australian Shale; Pourmand et al., 2012) normalized Ce ($[Ce]_{SN}$) against neighbouring non-redox-sensitive rare earth elements (REE). Due to the anomalous enrichments of La in seawater, the new proposed calculation without La proposed by Lawrence and Kamber. (2006) was adopted in this study: $Ce/Ce* = [Ce/(Pr \times$

192 (Pr/Nd))]$_{SN}$.

193 **4. Results**

194 *4.1. $CaCO_3$ content and major-element concentration*

195 The results (reported as means ± 1σ standard deviation) show that the percentage
196 $CaCO_3$ ranges from 79.8 to 99.5% (92.9 ± 5.2%, n = 70; Fig. 3). The pattern is one of a
197 gradual decrease up-section, starting at the onset level of the T-OAE CIE at −2 m,
198 continuing and culminating during the negative phase of the T-OAE CIE and almost going
199 back to background values at the end of the CIE interval. As illustrated in Fig. 3, the
200 elemental concentrations range from 42.5 to 376.9 ppm (125.9 ± 71.5 ppm, n = 67) for Al,
201 0 to 39.6 ppm (13.4 ± 8.7 ppm, n = 65) for Ti, 0.1 to 1.4 ppm (0.6 ± 0.3 ppm, n = 67) for
202 Th, and 0.4 to 5.6 ppm (2.2 ± 0.1 ppm, n = 66) for Sc, respectively. The profiles of Ti, Th,
203 and Sc show an abrupt positive shift at the Pliensbachian–Toarcian boundary, followed by
204 a very weak increase (Th and total REE) or relatively stable high-level values albeit with
205 small fluctuations (Ti and Sc) to around the mid-point of the CIE level (Fig. 3). They then
206 decrease gradually until the end-level of the CIE. By contrast, Al shows an overall increase
207 during the Pliensbachian–Toarcian boundary to the whole T-OAE CIE interval and
208 maintains relatively high values back at the end-level of the CIE. The manganese
209 concentrations in the Nianduo section range from ~23.1 to ~160.2 ppm (62.5 ± 32.8 ppm,
210 n = 67; Fig. 4). There is a decrease from ~80–120 to ~30 ppm below the Pliensbachian–
211 Toarcian boundary, closely followed by a gradual, slow increase to ~36–50 ppm around
212 the onset level of the T-OAE CIE, which becomes steeper to culminate within the negative
213 phase of the CIE and reaches high values around 80 ppm but with one datapoint of 160
214 ppm. Separated by a fall in Mn concentration (~33–44 ppm), the trend continues to increase

again up-section, culminating around the end-level of the T-OAE CIE with values around ~130 ppm before going back to background levels immediately above this point.

4.2. Trace-element concentration and Ce anomalies (Ce/Ce)*

The total REE (ΣREE) concentrations range from 2.8 to 75.8 ppm (25.7 ± 15.2 ppm, n = 67). The profile coincides with that of Ti, Th and Sc (Fig. 3). The PAAS-normalized patterns show that the REE distributions are characterized by extreme light REE (LREE) depletion, relative heavy REE (HREE) enrichment (Fig. 5A) apart from a few samples (marked as red dots in the curve of Fig. 3) and by a middle REE (MREE) enrichment (MREE-bulge or hat-shaped pattern; Fig. 5B). The Ce concentrations are 1.1–21.4 ppm (5.8 ± 4.3 ppm, n = 67) and paired Ce/Ce∗ values vary from 0.4 to 1.4 (0.9 ± 0.2, n = 67; Fig. 4). The Ce concentrations and Ce/Ce∗ both show an overall positive relationship with Mn, except for the overarching positive shift in the Ce/Ce∗ over the interval from −20.6 to −6.6 m without any changes in Ce and Mn concentrations.

5. Discussion

5.1. Elemental evidence for terrigenous input and evaluation of Ce cycling

There are a number of water-insoluble elements in seawater, such as Al, Ti, Th, Sc and REE, which mainly originate from chemical weathering by riverine water and/or dissolution of the chemically weathered product. Such elements have markedly higher concentrations in terrigenous detritus than do pure marine carbonates (Taylor and McLennan, 1985; Webb and Kamber, 2000; Frimmel, 2009). Therefore, the concentrations of water-insoluble elements in carbonate lattices, incorporated from ambient seawater, are sensitive to terrigenous influx, making these chemical species the ideal monitor for

237 continental chemical weathering (Frimmel, 2009; Zhao and Zheng, 2014; Li et al., 2017,
238 2019). In this study, the tempestites with silty or coarser siliciclastic fractions have been
239 excluded (see section 3.1) and the Nianduo section has relatively low TOC contents
240 (average value of 0.14 wt.%; Han et al., 2018). The compositions of analyzed samples are
241 thus mainly constituted by variable contents of carbonate and fine-grained clays deposited
242 under 'background' conditions, rather than abnormal contributions from storm-generated
243 input. As depicted in Fig. 3, the most water-insoluble Ti, Th, Sc and REE concentrations,
244 as well as Al (except the recovery interval of the T-OAE CIE), are positively correlated
245 with each other but negatively correlated with the carbonate content and presumably have
246 overall positive correlativity with clay. These observations suggest that these water-
247 insoluble elements mainly originate from clay minerals.

248 There are two major processes making contributions to the increase in water-insoluble
249 elements. Firstly, the siliciclastic components are more enriched in water-insoluble
250 elements than the carbonate minerals (Taylor and McLennan, 1985; Elderfield et al., 1990),
251 so that the dissolution of even minor siliciclastic materials during the acid leaching
252 procedure could greatly increase their concentrations and also mask the primary seawater
253 REE distribution patterns (Nothdurft et al. 2004). Secondly, the water-insoluble elements
254 from siliciclastic detritus may have been released and then incorporated into carbonate
255 minerals in an extensive open-system during early diagenesis, which could have increased
256 their concentrations while still retaining the main features of the REE distribution patterns
257 (e.g. Nothdurft et al., 2004; Azmy et al., 2011; Zhao and Zheng, 2014; Hood et al., 2018).

258 Regarding the possible contamination from leaching procedure mentioned above, a
259 threshold value of 1 ppm for Th and 4 ppm for Zr, corresponding to about 2% siliciclastic

contamination, has been used as an indicator of limited contamination from detrital sources (Frimmel, 2009; Franchi, 2018). In this study, the elemental concentrations range from 0.1 to 1.4 ppm (0.6 ± 0.3 ppm) for Th (Fig. 3) and from 0.1 to 4.8 ppm (1.5 ± 1.0 ppm) for Zr (see Supplementary material), which only have eight and one data points, respectively, higher than the threshold mentioned above. These observations suggest that only a few samples likely suffered siliciclastic contamination from the leaching procedure. Additionally, the $CaCO_3$ contents have an average of 92.88% and only five data points with paired elemental data are somewhat lower than 85% (Fig. 3), which is considered to be the lower limit that has the possibility of obscuring the REE from partial release of siliciclastic components (Tostevin et al., 2016; Cao et al., 2020). Most importantly, the PAAS-normalized REE patterns of most studied samples, even with relatively high Al, Ti, Th, Sc and REE contents, exhibit seawater-like REE patterns with LREE depletion, HREE enrichment, small positive Eu and La anomalies (Figs. 3 and 5A), all of which suggests primary preservation of the seawater signal (Kamber and Webb, 2001; Webb and Kamber, 2000; Nothdurft et al., 2004).

The remaining samples, characterized by the widely reported MREE-bulge or hat-shaped pattern (Fig. 5B), are also not likely to have been modified by siliciclastic contamination because they have overall lower contents of Al, Th and REE compared with stratigraphically adjacent samples (Fig. 3). The origin of this REE pattern still remains uncertain (see review by Zhao et al., 2021). The geochemical cut-off values are considered to be arbitrary and thus best applied on a case-by-case basis with multiple screening (Tostevin, 2021). Although a few samples have higher values in terrigenous input proxies than threshold and non-seawater-like REE patterns (Figs. 3 and 5B), other compelling

283 evidence suggests that the contamination from dissolution of terrigenous detritus during
284 the HAC leaching process is minimal. Therefore, the presence of fluids with high water-
285 insoluble element concentrations released from clays that originated from continental
286 weathering during early diagenesis could be the main mechanism, as envisaged in many
287 previous case studies (e.g. Nothdurft et al., 2004; Azmy et al., 2011; Zhao and Zheng, 2014;
288 Hood et al., 2018). In this case, the water-insoluble elements that have high concentrations
289 in siliciclastic detritus but low concentrations in carbonate lattice are ideal proxies to track
290 the terrigenous input (Zhao and Zheng, 2014).

291 Seawater REE patterns and associated Ce/Ce* in limestones are considered to be less
292 sensitive to post-depositional modification and therefore faithfully preserved because they
293 are structurally incorporated into carbonate, and REE/Ca ratios are relatively low in
294 diagenetic fluids (e.g. Webb and Kamber, 2000; Nothdurft et al., 2004; Webb et al., 2009;
295 Liu et al., 2019; Hood et al., 2018). However, caution must be applied when using water-
296 insoluble elements to trace the paleo-seawater composition, especially in cases where
297 carbonate is impure and siliciclastic contamination is obvious (Zhao and Zheng, 2014). In
298 this study, the seawater-like REE patterns of the overwhelming majority of samples offer
299 reliable evidence that the primary Ce/Ce* was preserved. Although minor REEs were
300 released from siliciclastic components during early diagenesis, the Ce has weak correlation
301 with Th (R^2 = 0.42; Fig. 6A), but is more closely coupled to Mn (R^2 = 0.63; Fig. 6B).
302 Additionally, the Mn has weak and no correlation with Th (R^2 = 0.39; Fig. 6C) and Sc (R^2
303 = 0.17; Fig. 6D), respectively. These observations suggest that the Ce signature is more
304 closely linked with redox-sensitive Mn behaviour, and neither of them is significantly
305 modified by interaction with siliciclastic detritus during early diagenesis.

306 *5.2. Climate-mediated enhanced continental weathering during the early Toarcian*

307 In the Nianduo section, continental weathering, indicated by water-insoluble elements
308 (Ti, Th, Sc and ΣREE), started to increase around Pliensbachian–Toarcian boundary time,
309 continued to rise weakly or maintained a relatively stable values during the negative phase
310 of the T-OAE CIE, and gradually returned to background levels over the recovery phase of
311 the CIE (Fig. 3). It is well known that changes in tectonism and paleoclimate are the two
312 dominant factors controlling continental weathering and thus associated with terrigenous
313 input into seawater by riverine freshwater (e.g., Kump and Arthur, 1997; Molnar, 2004).
314 During the Early Jurassic, the Tethys Himalaya was a mature and tectonically quiescent
315 passive continental margin situated at the northern edge of the Indian continent (Sciunnach
316 and Garzanti, 2012). Hence, regional tectonism and uplift is not likely to have been the
317 major cause of any increase in continental weathering in the study area.

318 Notably, the early Toarcian was characterized by the most extreme climatic and
319 environmental perturbations represented by the T-OAE as well as the preceding
320 Pliensbachian–Toarcian Boundary Event (PTBE): both phenomena associated with the
321 emplacement of the Karoo–Ferrar Large Igneous Province (e.g. Pálfy and Smith, 2000;
322 Cohen et al., 2004; Burgess et al., 2015; Percival et al., 2016; Al-Suwaidi et al., 2022),
323 which was likely the primary trigger. Terrigenous influx could have increased owing either
324 to enhanced chemical weathering during the period of global warming (Algeo and
325 Twitchett, 2010), and/or to enhanced physical weathering caused by sea-level fall during a
326 period of global cooling. Previous studies show that the PTBE was accompanied by an
327 ephemeral transgressive pulse, soon followed by a possible slight sea-level fall and then,
328 at the onset of the T-OAE CIE, by a rapid high-amplitude sea-level rise (e.g. Hallam,1981;

329 Hesselbo and Jenkyns 1998; Nikitenko et al., 2008; Ruebsam et al., 2019). However, only
330 the sea-level rise associated with the T-OAE was observed by carbonate microfacies
331 analysis in the Tethys Himalaya (Han et al., 2016). The evidence from oxygen-isotope
332 analysis of skeletal calcite together with distribution of possible high-latitude cold-
333 temperature deposits such as glendonites has been taken by some authors to suggest that
334 these sea-level changes over time scales of hundreds of thousands of years were mediated
335 by polar ice caps whose volume changed with global temperature (Suan et al., 2010; Dera
336 et al., 2011; Korte and Hesselbo, 2011; Ruebsam et al., 2019). However, the gradual
337 increase in water-insoluble elements in the Tibetan section does not correspond to such
338 putative transgressive-regressive-transgressive cycles in sea level over the PTBE to T-OAE
339 interval. Therefore, sea-level changes could not have played a critical role in increased
340 terrigenous influx during the early Toarcian.

341 Because the increase in terrigenous influx was not dominated by sea-level fall, the
342 accelerated chemical weathering associated with global warming and subsequent
343 transportation into seawater could be the causative mechanism (Cohen et al., 2004; Percival
344 et al., 2016; Them et al., 2017b; Kemp et al., 2020). It is well known that warm and wet
345 climates favor intense chemical weathering, which has been widely demonstrated over
346 short-term global warming events in the Phanerozoic (e.g. Cohen et al., 2004; Algeo and
347 Twitchett, 2010; Bottini et al., 2012; Pogge von Strandmann et al., 2013). Global warming,
348 as indicated by oxygen-isotope values in brachiopods and belemnites, started around
349 Pliensbachian–Toarcian boundary time and continued up to the T-OAE CIE (Suan et al.,
350 2010; Korte and Hesselbo, 2011; Korte et al., 2015; Müller et al., 2020). This
351 paleotemperature evolution is temporally consistent with the interval of rising values and

culminating ‘plateau’ of water-insoluble elements indicating enhanced continental weathering (Fig. 3) and also by strontium- and osmium-isotope profiles in sections from Europe, North America and Japan (Fig. 7; Cohen et al., 2004; Jenkyns, 2010; Ullmann et al., 2013; Percival et al., 2016; Them et al., 2017b; Kemp et al., 2020). The synchronous changes between these isotopic and elemental proxies for continental weathering suggest that rapid global warming drove an increase in this phenomenon globally, including the tropical zone of the Southern Hemisphere during the early Toarcian (Fig. 8A-C). Additionally, the recovery to background values of those proxies during the recovery phase of the CIE was also synchronous, indicating that enhanced organic-carbon burial could have gradually drawn down the CO_2 concentration and associated continental weathering intensity (Fig. 8D). However, the continuous increase in Al during the recovery T-OAE interval could also be ascribed to additional contribution of authigenic phases besides the increased continental weathering influx. For example, biogenic silica can be converted to authigenic aluminosilicates (Michalopoulos and Aller, 2004), in which the Al could be released and incorporated into carbonate, thereby increasing its concentration. Stratigraphically higher than the CIE interval, two short-term positive shifts of water-insoluble elements in the intervals of ~26–38 m and ~46–55 m were observed (Fig. 3), which might suggest additional pulses of enhanced continental weathering. However, corresponding sedimentary and carbon-isotope changes have not been observed over these two intervals in the Nianduo section, and there are also no obvious changes in multiple proxies immediately following the T-OAE CIE in the sections at Monte Sorgenza, Italy and Peniche, Portugal (Fig. 4). Therefore, these two pulses of elemental increase in the Nianduo section likely represent local signals whose cause is not clear based on the current data.

5.3. Redox condition of shallow waters during the early Toarcian

Manganese and cerium have been considered as useful proxies because they are sensitive to local–regional redox conditions and are widely used to track intermediate manganous (often referred to as suboxic), rather than fully anoxic, conditions in the shallow-water carbonate depositional environment (Jenkyns et al., 1991; Jenkyns, 2010; Lu et al., 2010; Sabatino et al., 2013; Tostevin et al., 2021). When bottom waters are oxygenated, Mn is transported to the seafloor in the form of Mn^{4+}/Mn^{3+} incorporated into (oxyhydr)oxides whereas when oxygen is depleted the Mn (oxyhydr)oxides previously deposited are reduced to soluble Mn^{2+} and then incorporated into crystal lattices of early diagenetic carbonate (Jenkyns et al., 1991; Huckriede and Meischner, 1996; de Baar et al., 2018). Ce^{3+} can be oxidized to insoluble Ce^{4+} and accumulate on the surface of Mn (oxyhydr)oxides and organic and clay particulate matter, or as discrete Ce oxide particles under oxygenated conditions, which leads to Ce depletion and negative Ce/Ce* in seawater (German et al., 1991; Bau et al., 1996; Byrne and Sholkovitz, 1996). By contrast, insoluble Ce^{4+} is transformed to soluble Ce^{3+} and released back into the water column under O_2-depleted suboxic conditions which leads to Ce enrichment and a positive Ce/Ce*. Therefore, an elevation in the sedimentary Mn and Ce concentration and positive Ce/Ce* is commonly considered to be an crucial stratigraphic marker for OAEs, and has been reported for the T-OAE, the early Aptian OAE 1a and OAE 2 at the Cenomanian–Turonian boundary (Jenkyns, 2010; Lu et al., 2010; Bodin et al., 2013).

Generally, a threshold value of 1 to define negative and positive Ce/Ce* is commonly applied to indicate oxygenated waters and conditions below the Mn redoxcline, respectively, but considered to be arbitrary, so many studies use the more conservative

range of < 0.8 and >1.2 (Tostevin et al., 2021 and references therein). In this study, the data mainly range between 0.8 and 1.2, suggesting no significant Ce/Ce* (Fig. 4), and thus only the general trend is discussed below. Although the reduction potential of Mn (1.23°V) is lower than Ce (1.61°V), both are sensitive to intermediate manganous conditions, and their redox cycling may behave similarly under low levels of oxygen (Canfield and Thamdrup, 2009; Tostevin et al., 2021). The expected positive correlation between them is indeed present (Figs. 4 and 6). Although carbonate is the host phase and any increase in its content could potentially make positive contributions to values of Mn and Ce, the concentrations of these two elements correlate negatively with carbonate content both in Nianduo (Fig. 7; this study) and Peniche (Hermoso et al., 2009b). Hence, the carbonate content of the sediment is not the dominant factor for the enrichment of these minor elements. By contrast, Monte Sorgenza in Italy is made up of relatively pure carbonate throughout the whole section (Lu et al., 2010), and therefore shifts in the normalized values of Mn/Ca and Ce/Ca should represent real changes.

Based on the characteristic negative CIE during the Pliensbachian–Toarcian transitional interval and T-OAE, we compare the obtained Mn and Ce data in this study with similar proxies from other sites (Fig. 4) in an attempt to reconstruct supra-regional or even global redox conditions in shallow waters. In the Nianduo section, the high-resolution Mn, Ce and Ce/Ce* overall show a persistent increase starting around the Pliensbachian–Toarcian boundary and culminating around the end-level of the T-OAE CIE. This trend can be subdivided into two increasing phases separated by a drop in values around the middle level of the CIE (a and b; Fig. 4). Similarly, the I/Ca data from the shallow-marine platform carbonates (Monte Sorgenza, Italy) show a two-pulse decrease, likely suggesting sequential

421 strong loss of oxygen causing reduction of dissolved iodate to iodide, which is not
422 incorporated into the carbonate lattice (Lu et al., 2010). By contrast, an overarching
423 positive shift of Mn/Ca, Ce/Ca and Ce/Ce* from Monte Sorgenza (Lu et al., 2010) and of
424 Mn from hemipelagic carbonates of Peniche, Portugal (Hermoso et al., 2009b) is observed
425 over the same stratigraphic interval. However, these profiles lack the falling trend
426 corresponding to the middle levels of the CIE, which could be ascribed to low resolution
427 and/or local factors. The corresponding shifts in Mn, Ce, Ce/Ce* and I/Ca from the
428 geographically separated sites of the shallow-water carbonate platforms of southern Tibet
429 (southeastern Tethys), Italy (western Tethys), and the hemipelagic successsion of Portugal
430 (junction between the westernmost Tethys and proto-Atlantic) reflects an enhanced global
431 fixation of Mn and Ce, likely characterized by two main pulses during the early Toarcian.
432 These observations suggest that oxygen-depleted (manganous) bottom waters at least
433 expanded along numerous Tethyan continental margins during the early Toarcian
434 beginning at the Pliensbachian–Toarcian boundary and continuing throughout the CIE
435 interval, albeit with a few fluctuations (Figs. 7 and 8A-D).

436 Recent evidence from redox-sensitive elements in bulk rock on the Adriatic Carbonate
437 Platform also confirm that oxygen-depleted waters expanded into shallow-water zones in
438 this area (Fig. 1; Ettinger et al., 2020). In this context, the dissolving Mn^{2+} and Ce^{3+} from
439 Mn (oxyhydr)oxides and Ce oxide reduction of previous deposits could have been an
440 important source for the diagenetic incorporation of these elements into the carbonate
441 lattice. Hence, the picture is one of Mn and Ce enrichment in Toarcian platform carbonates
442 of the greater Tethyan region driven by global redox change affecting relatively shallow
443 tropical waters. Such an interpretation is supported by coeval positive excursions in $\delta^{34}S$

444 of carbonate-associated sulfate from Yunjia and Wölong, southern Tibet (Fig. 7), Monte
445 Sorgenza, Italy, and also in thallium isotopes (ε^{205}Tl) from the European shelf sea and the
446 northeastern Panthalassan margin (Gill et al., 2011; Newton et al., 2011; Them et al., 2018;
447 Han et al., 2022), which suggest deoxygenation in the global ocean from Pliensbachian–
448 Toarcian boundary time onward. Notably, ε^{205}Tl shows two positive shfts at the same
449 stratigraphic interval as the Mn, Ce and Ce/Ce* excursions in the Nianduo section based
450 on the T-OAE CIE correlation, interpreted as due to massive reduction of global Mn
451 (oxyhydr)oxide deposition, which released the adsorbed heavier ε^{205}Tl isotope (Them et
452 al., 2018) and thus also the Ce. However, the sulfur and thallium isotopes do not
453 subsequently return to background values, as does I/Ca, so interpretations of isotopic
454 systems in terms of global redox post-dating the CIE remain ambiguous. By contrast, the
455 Mn enrichment occurred around Pliensbachian–Toarcian boundary time but returned to
456 background values following the onset of the CIE on the Adriatic Carbonate Platform
457 (Croatia) of western Tethys and in the Paris Basin of the north European shelf (Hermoso et
458 al., 2009b; Sabatino et al., 2013): a pattern that is stratigraphically coeval with the first
459 increasing Mn phase seen at Nianduo and Peniche. However, this earlier recovery is not
460 consistent with the results from Nianduo, Monte Sorgenza and Peniche, where the Mn
461 concentration returns to baseline around the end-level of the CIE (Fig. 4), possibly
462 representing a local signal.

463 According to the new data obtained in this study, the onset of increase in water-
464 insoluble elements at the Pliensbachian–Toarcian boundary lies stratigraphically
465 immediately below that of the redox-sensitive elements (Figs. 3, 4 and 7). This difference
466 in timing indicates that the first episode of shallow-water deoxygenation could be linked

467 to enhanced continental weathering and nutrient input, which increased primary
468 productivity and led to significant oxygen consumption, being most pronounced on the
469 deeper parts of the platform. By contrast, the gradual decline in water-insoluble elements
470 coincides with the elevation in redox-sensitive elements over the recovery phase of the CIE.
471 This pattern is consistent with the coeval relationship in isotopic records: a positive trend
472 in thallium isotopes and a move to less radiogenic values in osmium isotopes during this
473 stratigraphic interval (Cohen et al., 2004; Percival et al., 2016; Them et al., 2017b, 2018;
474 Kemp et al., 2020). Thus, the mechanism of enhanced continental weathering is not
475 applicable for this episode of deoxygenation (Fig. 8D). Significantly, this interval
476 corresponds to the high temperatures illustrated by oxygen isotopes and Mg:Ca ratios in
477 belemnites and TEX_{86} records from organic-rich shales from localities in Europe (e.g.
478 Bailey et al., 2003; Suan et al., 2010; Dera et al., 2011; Ruebsam et al., 2020; Jenkyns and
479 Macfarlane, 2022). Such temperature extremes, as well as playing a significant role in the
480 decrease in oxygen solubility, could have aided stratification of the water column and
481 dampened circulation. Alternatively, enhanced recycling of bioessential nutrients (e.g.
482 phosphorus) under more reducing conditions might have stimulated increased primary
483 productivity and resulted in deoxygenation, as also envisaged by Them et al. (2018).

484 *5.4. Carbonate crisis linked to enhanced continental weathering and deoxygenation*

485 During the late Pliensbachian–earliest Toarcian, *Lithiotis* bivalves and corals together
486 with other benthic faunas (foraminifera, gastropods, brachiopods, etc.) proliferated along
487 the entire tropical/subtropical Tethys Himalaya on the Kioto Platform where they
488 constructed major reef systems (e.g. Jadoul et al., 1998; Sciunnach and Garzanti, 2012;
489 Han et al., 2016, 2021; Fig. 8A-B). There were two major episodes of carbonate-platform

crisis along the southern Tethyan margin: at Pliensbachian–Toarcian boundary time and the early Toarcian (Bodin et al., 2010; Trecalli et al., 2012; Han et al., 2018; Ettinger et al., 2020; Krencker et al., 2020). The carbonate productivity crisis is directly illustrated by biotic extinction and obvious reduction of carbonate content. In the Nianduo section, the steadily decreasing trend in $CaCO_3$ (−3.6–0.4 m) from ~99 to ~95% coincides with the T-OAE CIE onset interval, followed by several periods of abrupt decline from ~96 to ~80% coinciding with the CIE negative phase itself (0.4–12.4 m; Fig. 7). Based on the data recently obtained from the Kioto Platform, the foraminiferal diversity and skeletal grain content started to decrease around the level of the Pliensbachian–Toarcian boundary, and decreased more severely during the negative phase of the T-OAE CIE (Figs. 2 and 7; Jiang et al., 2020; Han et al., 2021). Additionally, the *Lithiotis* bivalves, which were prominent framework builders in reef systems at that time, disappeared at the onset of the CIE (Han et al., 2018, 2021; Fig. 8C). Although the Kioto Platform suffered a severe crisis in benthic fauna, there were still a few smaller foraminifers present as sediment producers over the CIE interval (Han et al., 2018, 2021; Jiang et al., 2020) and resultant facies still contain a relatively high $CaCO_3$ content, suggesting a biotic platform that, albeit stressed, was not completely shut down (Fig. 8C-D). Overall, the environmental disturbances likely led to only minor modification of the Kioto carbonate factory at Pliensbachian–Toarcian boundary time, but played a more major role in triggering the subsequent early Toarcian benthic biotic crisis for carbonate producers. This progressive crisis of carbonate productivity is in agreement with observations in global sites from hemipelagic to shallow-marine settings (cf. Hesselbo et al., 2007; Sabatino et al., 2009; Hermoso et al., 2009b, 2012; Caruthers et al., 2014; Brame et al., 2019).

By contrast, an effective shutdown of most carbonate factories in the Moroccan Atlas and south-east France occurred at the Pliensbachian–Toarcian boundary, as confirmed by evidence of a significant drop in $CaCO_3$ content and abrupt shift from carbonates to siliciclastic deposits (Bodin et al., 2010; Léonide et al., 2012; Ait-Itto et al., 2018; Boulila et al., 2019; Krencker et al., 2020). Indeed, demise of a few biotic carbonate platforms occurred around Pliensbachian–Toarcian boundary time, whereas other resilient platforms continued growing and transitioned to comparatively unfossiliferous oolitic sedimentary systems or poorly fossiliferous deeper water micrites (Woodfine et al., 2008; Trecalli et al., 2012; Sabatino et al., 2013; Han et al., 2018; Ettinger et al., 2020). Multiple not mutually exclusive mechanisms can explain the global carbonate production crisis, including oceanic anoxia and acidification, temperature excess and sea-level rise, enhanced terrigenous input and eutrophication (Jenkyns, 2010 and Hu et al., 2020 for a review). However, these mechanisms most likely played variable roles in different basins and time intervals during the late Pliensbachian–early Toarcian, and generally acted in concert with local factors. In Tibetan sections, the rapid sea-level rise and platform crisis, including biota and carbonate productivity, correlates very well with the onset of the T-OAE CIE (Fig. 7). Nevertheless, carbonate sedimentation on a healthy and highly productive platform should have been fast enough to catch up with this rise in sea level (Godet, 2013; Han et al., 2018). Furthermore, *Lithiotis* was also not observed in the CIE interval on the Campania–Lucania Platform in southern Italy where paleowater depth did not change, albeit with a shift from a dominantly skeletal to non-skeletal oolitic deposition (Trecalli et al., 2012). Therefore, extinction of *Lithiotis*-dominated benthic assemblages and the associated hyper-calcifying carbonate productivity crisis were likely not linked to sea-level change.

In this study, an increase in Al, Sc, Th and REE in the Kioto Platform is first registered around the Pliensbachian–Toarcian boundary, immediately preceding the elevation in Mn, Ce and Ce/Ce* (Figs. 3, 4 and 7). Hence, the almost synchronously enhanced terrigenous influx and deoxygenation over this time interval likely led to the slight decrease in foraminiferal diversity, carbonate content and skeletal abundance in the Tethys Himalaya (Fig. 7). Subsequently, these proxies show a synchronous rapid large rise at the onset level of the T-OAE CIE, where the macrobenthic communities including benthic foraminifera (Figs. 2 and 7) and carbonate content show a significant decrease, and the reef-building *Lithiotis* disappear (Figs. 3, 7 and 8A-C), suggesting an associated carbonate-platform crisis. These observations and relationship demonstrate that the drastically enhanced terrigenous flux and deoxygenation, in response to the pulse of rapid massive carbon release in the early Toarcian, likely played a pivotal role in causing deterioration of ecological conditions and triggering a biotic crisis for benthic carbonate producers dominated by *Lithiotis*. Obviously, the terrigenous flux into carbonate platforms had strong local variability because visible siliciclastic deposits were observed both around the Pliensbachian–Toarcian boundary and lower Toarcian in Morocco (Bodin et al., 2010; Krencker et al., 2015, 2020), but not in Tibet. This study shows that it is necessary to seek characteristic geochemical proxies of terrigenous input (e.g. Al, Ti, Th, Sc and REE) from isolated carbonate platforms (e.g. Italy, Slovenia, and Croatia in western Tethys), which were not directly influenced by continental riverine inputs to assess possible global similarities. Changes in redox proxies on the Adriatic and Campania–Lucania (e.g. Monte Sorgenza) Platforms (Lu et al., 2010; Ettinger et al., 2020) and also the Kioto Platform indicate that oxygen depletion in shallow waters immediately preceding or coincident with

559 the biotic carbonate platform crisis was likely ubiquitous along the southern Tethyan
560 margin, potentially having profoundly negative effects on carbonate producers and
561 sedimentation.

562 **6. Conclusions**

563 The major and trace elements in carbonates from the Kioto Carbonate Platform in
564 Tibet provide unique insights on palaeoceanographic changes in shallow tropical waters
565 during the late Pliensbachian–early Toarcian interval and help elucidate potential triggers
566 for the crisis in the carbonate factory. The synchronous rise in most water-insoluble
567 elements (e.g. Al, Ti, Th, Sc and REE), starting at the Pliensbachian–Toarcian boundary
568 and continuing during the negative phase of the T-OAE CIE, suggests enhanced terrigenous
569 influx into the shallow-marine system, which was likely induced by global warming and
570 associated enhanced continental weathering. A slight enrichment in Mn, Ce and Ce/Ce*
571 occurs immediately following the onset of increase in water-insoluble elements, which then
572 passes stratigraphically upward into higher values in coincidence with the elevation in
573 water-insoluble elements during the negative phase of the T-OAE CIE. These observations
574 are compatible with the hypothesis that deoxygenation in shallow waters during this time
575 interval could be linked to enhanced continental weathering and nutrient input, favoring
576 relatively elevated primary productivity and oxygen consumption. By contrast, the water-
577 insoluble elements (except Al) show a gradual decreasing trend superimposed upon the
578 second positive shift of redox proxies during the recovery phase of the CIE. In this instance,
579 the decline in continental weathering intensity corresponded with the second phase of
580 deoxygenation in shallow waters. This deoxygenation could be ascribed to local
581 stratification of the water column or enhanced recycling of bioessential nutrients and

increased primary productivity. The relationship between carbonate content and proxies for terrigenous influx and deoxygenation, with biotic data of *Lithiotis* bivalves and foraminifera, and skeletal grain content suggests that enhanced terrigenous influx and deoxygenation likely led to slight modification of the Kioto carbonate factory around Pliensbachian–Toarcian boundary time and played an ensuing pivotal role in a more severe crisis for benthic carbonate producers during the early Toarcian, coincident with the T-OAE negative CIE. Such a mechanism is also likely applicable for other coeval carbonate platforms in the western Tethys.

Acknowledgements

Our thanks go to Zhifei Liu at Tongji University for carbonate determinations. We thank Juan Li and Bo Zhou for their help in the field, Yiwei Xu for his assistance in the laboratory, Fei Li for his helpful discussion, and two anonymous reviewers for their constructive comments. This work was funded by the National Natural Science Foundation of China (NSFC; Grant Nos. 42002121, 41888101 and 41525007), and a research grant (2021-LAMD-K03) from the State Key Laboratory of Mineral Deposit Research of Nanjing University. This manuscript is a contribution to the IGCP 739.

Figure captions

Fig. 1. (A) Toarcian global paleogeographic map (~179.3 Ma, Scotese, 2014) and (B) geological sketch map of the Himalaya showing the studied section, modified after Hu et al. (2016). Abbreviations: GCT: Great Counter Thrust; STDZ: South Tibetan Detachment Zone; MCT: Main Central Thrust; MBT: Main Boundary Thrust; MFT: Main Frontal Thrust; H: High Atlas Carbonate Platform, Morocco; C: Campania–Lucania Carbonate Platform, Italy; A: Adriatic Carbonate Platform, Croatia and Slovenia.

Fig. 2. Outcrop photographs and characteristic carbonate microfacies of analyzed samples. (A) Nianduo section showing the boundary (abrupt facies change) of the Pupuga and Nieniexiongla Formations; (B) Off-white, medium/thick-bedded limestones of the Pupuga Formation; (C) Dark grey, thin-bedded limestones of the Nieniexiongla Formation; (D) Ooid grainstone (−22.6 m); (E) Lump grainstone (−3.6 m); (F) Bioclastic packstone/wackestone (−15.6 m); (G) Bioclastic wackestone (−19.6 m); (H) Peloid packstone (1.4 m); (I) Mudstone (5.6 m). Note that the terminology "mudstone" refers to a type of limestone, as defined by Dunham (1962), and not indicative of siliciclastic sediment.

Fig. 3. Systematic variations in geochemical profiles for $\delta^{13}C_{TOC}$ (Han et al., 2018), $CaCO_3$ content, and the carbonate-hosted water-insoluble elements Al, Ti, Th, Sc and total REE over the upper Pliensbachian–lower Toarcian interval of the Nianduo section. Note that (1) the orange curve represents the 3-point moving average in the $\delta^{13}C_{TOC}$ profile, as well as in the Wölong section (Fig. 7), and (2) the black and red dots in elemental profiles respectively represent samples with the seawater-like (Fig. 5A) and the MREE-bulge/hat-shaped (Fig. 5B) pattern of REE distribution. Pl–To: Pliensbachian–Toarcian.

Fig. 4. Correlation of geochemical profiles of commonly used redox proxies in upper Pliensbachian–lower Toarcian carbonates from eastern and western Tethys and the northern Europe shelf. The Mn, and Ce and Ce/Ce* ($[Ce/(Pr \times (Pr/Nd))]_{SN}$) data of the Nianduo section are from this study. Two sequential increasing phases (a and b) of redox proxies separated by a drop in values around the middle level of the CIE are present in the Nianduo section. For the platform carbonates of Monte Sorgenza (Italy), $\delta^{13}C_{TOC}$ data are from Trecalli et al. (2012), Mn/Ca, Ce/Ca and Ce/Ce* ($(\log[3Ce/(2La + Nd)]_{SN})$) data are from Lu et al. (2010); for the hemipelagic marls of Peniche (Portugal), $\delta^{13}C_{carb}$ data are from

628 Hesselbo et al. (2007) with Mn data from Hermoso et al. (2009b). Detailed lithological key
629 as in Fig. 3.

630 **Fig. 5**. PAAS-normalized REE distribution pattern of HAC-leaching solution for upper
631 Pliensbachian–lower Toarcian carbonates from the Nianduo section. A. seawater-like REE
632 pattern in this study and modern deep Pacific oxic seawater (red line), modified after Alibo
633 and Nozaki (1999); B. MREE-bulge or hat-shaped pattern (sample points marked as red in
634 curve shown in Fig. 3).

635 **Fig. 6**. Cross-plots of elements from HAC-leaching solution. Ce *versus* Th (A, $R^2 = 0.42$)
636 and Mn (B, $R^2 = 0.63$); Mn *versus* Th (C, $R^2 = 0.39$) and Sc (D, $R^2 = 0.17$).

637 **Fig. 7**. Comprehensive paleoenvironmental and biotic data from the upper Pliensbachian–
638 lower Toarcian of the Kioto Carbonate Platform in the Tibetan Himalaya and the Mochras
639 borehole in UK. In Tibet, the $\delta^{13}C_{TOC}$ data are from Han et al. (2018), foraminiferal
640 diversity (blue and grey shaded area respectively representing larger and smaller benthic
641 foraminifera) from Jiang et al. (2020), skeletal grain (Sg) content from Han et al. (2021)
642 and sulfur-isotope values ($\delta^{34}S_{CAS}$) of carbonate-associated sulfate from Newton et al.
643 (2011) (black, Yunjia section) and Han et al. (2022) (green, Wölong section). The $\delta^{13}C_{TOC}$
644 and $^{187}Os/^{188}Os_i$ data of the Mochras Borehole are from Percival et al. (2016). Note that the
645 Wölong section is ~500 metres away from the Yunjia section and the geochemical data
646 from these two sections can be readily combined based on carbon-isotope correlation (Han
647 et al., 2021, 2022). Lithological and foraminiferal key and other details as in Fig. 3 and 8A.

648 **Fig. 8**. Interpretative reconstructions of the deoxygenation and changes in continental
649 weathering on the shallow-water Kioto Carbonate Platfrom during the Pliensbachian–
650 Toarcian transitional interval in what is now southern Tibet. The proposed depositional

model for the Kioto carbonate platform and lhe ocation of the Nianduo section is modified from the comprehensive data of Han et al. (2016, 2018) and Jiang et al. (2021). Note that: (1) the depositional environment abruptly changed from shallow-water carbonate platform (A and B) to deeper-water carbonate ramp (C and D) due to the sea-level rise and carbonate-platform crisis at the onset of the T-OAE CIE, and (2) the green arrows indicate the expansion of oxygen-depleted water.

References

Ait-Itto, F.-Z., Martinez, M., Price, G.D., Ait Addi, A., 2018. Synchronization of the astronomical time scales in the Early Toarcian: A link between anoxia, carbon-cycle perturbation, mass extinction and volcanism. Earth Planet. Sci. Lett. 493, 1–11.

Algeo, T.J., Twitchett, R.J., 2010. Anomalous Early Triassic sediment fluxes due to elevated weathering rates and their biological consequences. Geology 38, 1023–1026.

Alibo, D.S., Nozaki, Y., 1999. Rare earth elements in seawater: particle association, shale-normalization, and Ce oxidation. Geochim. Cosmochim. Ac. 63, 363–372.

Al-Suwaidi, A.H., Ruhl, M., Jenkyns, H.C., Damborenea, S.E., Manceñido, M.O., Condon, D.J., Angelozzi, G.N., Kamo, S.L., Storm, M., Riccardi, A.C., Hesselbo, S.P., 2022. New age constraints on the Lower Jurassic Pliensbachian–Toarcian Boundary at Chacay Melehue (Neuquén Basin, Argentina). Scientific Reports, 12, 4975.

Azmy, K., Brand, U., Sylvester, P., Gleeson, S.A., Logan, A., Bitner, M.A., 2011. Biogenic and abiogenic low-Mg calcite (bLMC and aLMC): Evaluation of seawater-REE composition, water masses and carbonate diagenesis. Chem. Geol. 280, 180–190.

Bailey, T.R., Rosenthal, Y., McArthur, J.M., van de Schootbrugge, B., Thirlwall, M.F., 2003. Paleoceanographic changes of the Late Pliensbachian-Early Toarcian interval: a

possible link to the genesis of an Oceanic Anoxic Event. Earth Planet. Sci. Lett. 212, 307–320.

Bau, M., Koschinsky, A., Dulski, P., Hein, J.R., 1996. Comparison of the partitioning behaviours of yttrium, rare earth elements, and titanium between hydrogenetic marine ferromanganese crusts and seawater. Geochim. Cosmochim. Acta 60, 1709–1725.

Bodin, S., Godet, A., Westermann, S., Föllmi, K.B., 2013. Secular change in northwestern Tethyan water-mass oxygenation during the late Hauterivian–early Aptian. Earth Planet. Sci. Lett. 374, 121–131.

Bodin, S., Mattioli, E., Frohlich, S., Marshall, J.D., Boutib, L., Lahsini, S., Redfern, J., 2010. Toarcian carbon isotope shifts and nutrient changes from the Northern margin of Gondwana (High Atlas, Morocco, Jurassic): palaeoenvironmental implications. Palaeogeogr. Palaeoclimatol. Palaeoecol. 297, 377–390.

Bottini, C., Cohen, A.S., Erba, E., Jenkyns, H.C., Coe, A.L., 2012. Osmium-isotope evidence for volcanism, weathering, and ocean mixing during the early Aptian OAE 1a. Geology 40, 583–586.

Boulila, S., Galbrun, B., Sadki, D., Gardin, S., Bartolini, A., 2019. Constraints on the duration of the early Toarcian T-OAE and evidence for carbon-reservoir change from the High Atlas (Morocco). Global. Planet. Change 175, 113–128.

Brame, H.M.R., Martindale, R.C., Ettinger, N.P., Debeljak, I., Vasseur, R., Lathuiliere, B., Kabiri, L., Bodin, S., 2019. Stratigraphic distribution and paleoecological significance of Early Jurassic (Pliensbachian-Toarcian) lithiotid-coral reefal deposits from the Central High Atlas of Morocco. Palaeogeogr. Palaeoclimatol. Palaeoecol. 514, 813–837.

Brazier, J.M., Suan, G., Tacail, T., Simon, L., Martin, J.E., Mattioli, E., Baiter, V., 2015. Calcium isotope evidence for dramatic increase of continental weathering during the Toarcian oceanic anoxic event (Early Jurassic). Earth Planet. Sci. Lett. 411, 164–176.

Burgess, S.D., Bowring, S.A., Fleming, T.H., Elliot, D.H., 2015. High-precision geochronology links the Ferrar large igneous province with early-Jurassic ocean anoxia and biotic crisis. Earth Planet. Sci. Lett. 415, 90–99.

Byrne, R.H., Sholkovitz, E.R., 1996. Marine chemistry and geochemistry of the lanthanides. In: Handbook on the Physics and Chemistry of Rare Earths. 23. pp. 497–593.

Canfield, D.E., Thamdrup, B., 2009. Towards a consistent classification scheme for geochemical environments, or, why we wish the term 'suboxic' would go away. Geobiology 7, 385–392.

Cao, C., Liu, X.-M., Bataille, C.P., Liu, C., 2020. What do Ce anomalies in marine carbonates really mean? A perspective from leaching experiments. Chem. Geol. 532, 119413.

Caruthers, A.H., Smith, P.L., Gröcke, D.R., 2014. The Pliensbachian–Toarcian (Early Jurassic) extinction: A North American perspective. In: Keller, G. and Kerr, A.C., Eds, Volcanism, Impacts, and Mass Extinctions: Causes and Effects, Geological Society of America Special Papers 505, 225–243.

Caswell, B.A., Coe, A.L., 2014. The impact of anoxia on pelagic macrofauna during the Toarcian Oceanic Anoxic Event (Early Jurassic). Proceedings Geologists' Assoc. 125, 383–391.

Cohen, A.S., Coe, A.L., Harding, S.M., Schwark, L., 2004. Osmium isotope evidence for

the regulation of atmospheric CO_2 by continental weathering. Geology 32, 157–160.

de Baar, H.J.W., Bruland, K.W., Schijf, J., van Heuven, S.M.A.C., Behrens, M.K., 2018. Low cerium among the dissolved rare earth elements in the central North Pacific Ocean. Geochim. Cosmochim. Acta 236, 5–40.

Dera, G., Brigaud, B., Monna, F., Laffont, R., Puceat, E., Deconinck, J.F., Pellenard, P., Joachimski, M.M., Durlet, C., 2011. Climatic ups and downs in a disturbed Jurassic world. Geology 39, 215–218.

Dickson, A.J., Gill, B.C., Ruhl, M., Jenkyns, H.C., Porcelli, D., Idiz, E., Lyons, T.W., van den Boorn, S., 2017. Molybdenum-isotope chemostratigraphy and paleoceanography of the Toarcian Oceanic Anoxic Event (Early Jurassic). Paleoceanography 32, 813–829.

Dunham, R.J., 1962. Classification of carbonate rocks according to depositional texture. In: Ham, W.E. (Ed.) Classification of carbonate rocks, AAPG Memoir, 1. pp. 108–121.

Elderfield, H., Upstill-Goddard, R., Sholkovitz, E.R., 1990. The rare earth elements in rivers, estuaries, and coastal seas and their significance to the composition of ocean waters. Geochim. Cosmochim. Acta 54, 971–991.

Ettinger, N.P., Larson, T.E., Kerans, C., Thibodeau, A.M., Hattori, K.E., Kacur, S.M., Martindale, R.C., 2020. Ocean acidification and photic-zone anoxia at the Toarcian Oceanic Anoxic Event: Insights from the Adriatic Carbonate Platform. Sedimentology 68, 63–107.

Föllmi, K.B., Godet, A., Bodin, S., Linder, P., 2006. Interactions between environmental change and shallow water carbonate buildup along the northern Tethyan margin and

743 their impact on the Early Cretaceous carbon isotope record. Paleoceanography 21,
744 PA4211. https:// doi: 10.1029/2006PA001313.
745 Franchi, F., 2018. Petrographic and geochemical characterization of the Lower Transvaal
746 Supergroup stromatolitic dolostones (Kanye Basin, Botswana). Precambrian Res. 310,
747 93–113.
748 Frimmel, H.E., 2009. Trace element distribution in Neoproterozoic carbonates as
749 palaeoenvironmental indicator. Chem. Geol. 258, 338–353.
750 German, C.R., Holliday, B.P., Elderfield, H., 1991. Redox cycling of rare earth elements in
751 the suboxic zone of the Black Sea. Geochim. Cosmochim. Ac. 55, 3553–3558.
752 Gill, B.C., Lyons, T.W., Jenkyns, H.C., 2011. A global perturbation to the sulfur cycle
753 during the Toarcian Oceanic Anoxic Event. Earth Planet. Sci. Lett. 312, 484–496.
754 Godet, A., 2013. Drowning unconformities: Palaeoenvironmental significance and
755 involvement of global processes. Sediment. Geol. 293, 45–66.
756 Hallam, A., 1981. A revised sea-level curve for the early Jurassic. J. Geol. Soc. Lond. 138,
757 735–743.
758 Han, Z., Hu, X., BouDagher-Fadel, M., Jenkyns, H.C., Franceschi, M., 2021. Early Jurassic
759 carbon-isotope perturbations in a shallow water succession from the Tethys Himalaya,
760 southern hemisphere. Newsl. Stratigr. 54, 461–481.
761 Han, Z., Hu, X., He, T., Newton, R.J., Jenkyns, H.C., Jamieson, R.A., Franceschi, M., 2022.
762 Early Jurassic long-term oceanic sulfur-cycle perturbations in the Tibetan Himalaya.
763 Earth Planet. Sci. Lett. 578, 117261.
764 Han, Z., Hu, X., Kemp, D.B., Li, J., 2018. Carbonate-platform response to the Toarcian
765 Oceanic Anoxic Event in the southern hemisphere: Implications for climatic change

766 and biotic platform demise. Earth Planet. Sci. Lett. 489, 59–71.
767 Han, Z., Hu, X., Li, J., Garzanti, E., 2016. Jurassic carbonate microfacies and relative sea-
768 level changes in the Tethys Himalaya (southern Tibet). Palaeogeogr. Palaeoclimatol.
769 Palaeoecol. 456, 1–20.
770 Harries, P.J., Little, C.T., 1999. The early Toarcian (Early Jurassic) and the Cenomanian–
771 Turonian (Late Cretaceous) mass extinctions: similarities and contrasts. Palaeogeogr.
772 Palaeoclimatol. Palaeoecol. 154, 39–66.
773 Hermoso, M., Le Callonnec, L., Minoletti, F., Renard, M. and Hesselbo, S.P., 2009a.
774 Expression of the Early Toarcian negative carbon-isotope excursion in separated
775 carbonate microfractions (Jurassic, Paris Basin). Earth Planet. Sci. Lett. 277, 194–203.
776 Hermoso, M., Minoletti, F., Le Callonnec, L., Jenkyns, H.C., Hesselbo, S.P., Rickaby,
777 R.E.M., Renard, M., de Rafelis, M., Emmanuel, L., 2009b. Global and local forcing
778 of Early Toarcian seawater chemistry: A comparative study of different
779 paleoceanographic settings (Paris and Lusitanian basins). Paleoceanography 24,
780 PA4208. https://doi:10.1029/2009PA001764
781 Hermoso, M., Minoletti, F., Rickaby, R.E.M., Hesselbo, S.P., Baudin, F., Jenkyns, H.C.,
782 2012. Dynamics of a stepped carbon-isotope excursion: Ultra high-resolution study of
783 Early Toarcian environmental change. Earth Planet. Sci. Lett. 319, 45–54.
784 Hesselbo, S.P., Gröcke, D.R., Jenkyns, H.C., Bjerrum, C.J., Farrimond, P., Morgans Bell,
785 H.S., Green, O.R., 2000. Massive dissociation of gas hydrate during a Jurassic oceanic
786 anoxic event. Nature 406, 392–395.
787 Hesselbo, S.P., Jenkyns, H.C., 1998. British Lower Jurassic sequence stratigraphy. In: de
788 Graciansky, P.-C., Hardenbol, J., Jacquin, T., Vail, P.R. (Eds), Mesozoic and Cenozoic

Sequence Stratigraphy of European Basins, Special Publication Society for Sedimentary Geology (SEPM) 60, 561–581.

Hesselbo, S.P., Jenkyns, H.C., Duarte, L.V., Oliveira, L.C.V., 2007. Carbon-isotope record of the Early Jurassic (Toarcian) Oceanic Anoxic Event from fossil wood and marine carbonate (Lusitanian Basin, Portugal). Earth Planet. Sci. Lett. 253, 455–470.

Hood, A.v.S., Planavsky, N.J., Wallace, M.W., Wang, X., 2018. The effects of diagenesis on geochemical paleoredox proxies in sedimentary carbonates. Geochim. Cosmochim. Acta 232, 265–287.

Hu, X., Li, J., Han, Z., Li, Y., 2020. Two types of hyperthermal events in the Mesozoic–Cenozoic: Environmental impacts, biotic effects, and driving mechanisms. Sci. China. Earth. Sci. 63, 1–18.

Hu, X., Wang, J., Boudagher-Fadel, M., Garzanti, E., An, W., 2016. New insights into the timing of the India – Asia collision from the Paleogene Quxia and Jialazi formations of the Xigaze forearc basin, South Tibet. Gondwana Res. 32, 76–92.

Huckriede, H., Meischner, D., 1996. Origin and environment of manganese-rich sediments within black-shale basins. Geochim. Cosmochim. Acta 60, 1399–1413.

Jadoul, F., Berra, F., Garzanti, E., 1998. The Tethys Himalayan passive margin from Late Triassic to Early Cretaceous (South Tibet). J. Asian. Earth. Sci. 16, 173–194.

Jenkyns, H.C., 1988. The early Toarcian (Jurassic) anoxic event; stratigraphic, sedimentary and geochemical evidence. Am. J. Sci. 288, 101–151.

Jenkyns, H.C., Clayton, C.J., 1997. Lower Jurassic epicontinental carbonates and mudstones from England and Wales: chemostratigraphic signals and the early Toarcian anoxic event. Sedimentology 44, 687–706.

812 Jenkyns, H.C., 2010. Geochemistry of oceanic anoxic events. Geochem. Geophys. Geosyst.
813 11, Q03004, doi: 10.1029/2009GC002788. .
814 Jenkyns, H.C., 2020. The demise and drowning of Early Jurassic (Sinemurian) carbonate
815 platforms: stratigraphic evidence from the Italian peninsula, Sicily and Spain. In: l'
816 Eredità scientifica di Paolo Scandone, Geologo, Atti del Convegni Lincei, 335, 55–
817 82.
818 Jenkyns, H.C., Macfarlane, S., 2022. The chemostratigraphy and environmental
819 significance of the Marlstone and Junction Bed (Beacon Limestone, Toarcian, Lower
820 Jurassic, Dorset, UK). Geol. Mag. 159, 357–371.
821 Jenkyns, H.C., Géczy, B., Marshall, J.D., 1991. Jurassic manganese carbonates of Central
822 Europe and the early Toarcian Anoxic Event. J. Geol. 99, 137–149.
823 Jenkyns, H.C., Gröcke, D.R., Hesselbo, S.P., 2001. Nitrogen isotope evidence for water
824 mass denitrification during the early Toarcian (Jurassic) oceanic anoxic event.
825 Paleoceanography, 16, 593–603.
826 Jiang, S., Song, H., Kemp, D.B., Dai, X., Liu, X., 2020. Two pulses of extinction of larger
827 benthic foraminifera during the Pliensbachian–Toarcian and early Toarcian
828 environmental crises. Palaeogeogr. Palaeoclimatol. Palaeoecol. 560, 109998.
829 Kamber, B.S., Webb, G.E., 2001. The geochemistry of late Archaean microbial carbonate:
830 implications for ocean chemistry and continental erosion history. Geochim.
831 Cosmochim. Acta 65, 2509–2525.
832 Kemp, D.B., Selby, D., Izumi, K., 2020. Direct coupling between carbon release and
833 weathering during the Toarcian oceanic anoxic event. Geology 48, 976–980.
834 Korte, C., Hesselbo, S.P., 2011. Shallow marine carbon and oxygen isotope and elemental

records indicate icehouse-greenhouse cycles during the Early Jurassic. Paleoceanography 26, PA4219. https:// doi:10.1029/2011PA002160.

Korte, C., Hesselbo, S.P., Ullmann, C.V., Dietl, G., Ruhl, M., Schweigert, G., Thibault, N., 2015. Jurassic climate mode governed by ocean gateway. Nat. Commun. 6, 10015.

Kraft, S., Frank, M., Hathorne, E.C., Weldeab, S., 2013. Assessment of seawater Nd isotope signatures extracted from foraminiferal shells and authigenic phases of Gulf of Guinea sediments. Geochim. Cosmochim. Acta 121, 414–435.

Krencker, F.N., Bodin, S., Suan, G., Heimhofer, U., Kabiri, L., Immenhauser, A., 2015. Toarcian extreme warmth led to tropical cyclone intensification. Earth Planet. Sci. Lett. 425, 120–130.

Krencker, F.-N., Fantasia, A., Danisch, J., Martindale, R., Kabiri, L., El Ouali, M., Bodin, S., 2020. Two-phased collapse of the shallow-water carbonate factory during the late Pliensbachian–Toarcian driven by changing climate and enhanced continental weathering in the Northwestern Gondwana Margin. Earth-Sci. Rev. 208, 103254.

Kump, L.R., Arthur, M.A., 1997. Global Chemical Erosion during the Cenozoic: Weatherability Balances the Budgets. In Tectonic Uplift and Climate Change (ed. W. F. Ruddiman). Plenum Press, New York, pp. 399–426.

Lawrence, M.G., Kamber, B.S., 2006. The behaviour of the rare earth elements during estuarine mixing—revisited. Marine Chemi. 100, 147–161.

Léonide, P., Floquet, M., Durlet, C., Baudin, F., Pittet, B., Lecuyer, C., 2012. Drowning of a carbonate platform as a precursor stage of the Early Toarcian global anoxic event (Southern Provence sub-Basin, South-east France). Sedimentology 59, 156–184.

Li, W., Zheng, Y., Zhao, Y., 2017. Geochemical evidence from marine carbonate for

858 enhanced terrigenous input into seawater during the Ediacaran-Cambrian transition in
859 South China. Precambrian Res. 291, 83–97.
860 Liu, X., Hardisty, D.S., Lyons, T.W., Swart, P.K., 2019. Evaluating the fidelity of the cerium
861 paleoredox tracer during variable carbonate diagenesis on the Great Bahamas Bank.
862 Geochim. Cosmochim. Acta 248, 25–42.
863 Lu, Z.L., Jenkyns, H.C., Rickaby, R.E.M., 2010. Iodine to calcium ratios in marine
864 carbonate as a paleo-redox proxy during oceanic anoxic events. Geology 38, 1107–
865 1110.
866 McArthur, J.M., Donovan, D.T., Thirlwall, M.F., Fouke, B.W., Mattey, D., 2000. Strontium
867 isotope profile of the early Toarcian (Jurassic) oceanic anoxic event, the duration of
868 ammonite biozones, and belemnite palaeotemperatures. Earth Planet. Sci. Lett. 179,
869 269–285.
870 Michalopoulos, P., Aller, R.C. 2004. Early diagenesis of biogenic silica in the Amazon delta:
871 alteration, authigenic clay formation, and storage. Geochim. Cosmochim. Acta 68,
872 1061–1085.
873 Molnar, P., 2004. Late Cenozoic increase in accumulation rates of terrestrial sediment: how
874 might climate change have affected erosion rates? Annu. Rev. Earth. Plan. Sci. 32,
875 67–89.
876 Müller, T., Jurikova, H., Gutjahr, M., Tomašových, A., Schlögl, J., Liebetrau, V., Duarte,
877 L.v., Milovský, R., Suan, G., Mattioli, E., Pittet, B., Eisenhauer, A., 2020. Ocean
878 acidification during the early Toarcian extinction event: Evidence from boron isotopes
879 in brachiopods. Geology 48, 1184–1188.
880 Newton, R.J., Reeves, E.P., Kafousia, N., Wignall, P.B., Bottrell, S.H., Sha, J.-G., 2011.

881 Low marine sulfate concentrations and the isolation of the European epicontinental
882 sea during the Early Jurassic. Geology 39, 7–10.
883 Nikitenko, B., Shurygin, B., Mickey, M., 2008. High resolution stratigraphy of the Lower
884 Jurassic and Aalenian of Arctic regions as the basis for detailed palaeobiogeographic
885 reconstructions. Norw. J. Geol. 88, 267–278.
886 Nothdurft, L.D., Webb, G.E., Kamber, B.S., 2004. Rare earth element geochemistry of Late
887 Devonian reefal carbonates, Canning Basin, Western Australia: confirmation of a
888 seawater REE proxy in ancient limestones. Geochim. Cosmochim. Acta 68, 263–283.
889 Pálfy, J., Smith, P.L., 2000. Synchrony between Early Jurassic extinction, oceanic anoxic
890 event, and the Karoo–Ferrar flood basalt volcanism. Geology 28, 747–750.
891 Percival, L.M.E., Cohen, A.S., Davies, M.K., Dickson, A.J., Hesselbo, S.P., Jenkyns, H.C.,
892 Leng, M.J., Mather, T.A., Storm, M.S., Xu, W., 2016. Osmium isotope evidence for
893 two pulses of increased continental weathering linked to Early Jurassic volcanism and
894 climate change. Geology 44, 759–762.
895 Percival, L.M.E., Witt, M.L.I., Mather, T.A., Hermoso, M., Jenkyns, H.C., Hesselbo, S.P.,
896 Al-Suwaidi, A.H., Storm, M.S., Xu, W., Ruhl, M., 2015. Globally enhanced mercury
897 deposition during the end-Pliensbachian extinction and Toarcian OAE: A link to the
898 Karoo–Ferrar Large Igneous Province. Earth Planet. Sci. Lett. 428, 267–280.
899 Pogge von Strandmann, P.A.E., Jenkyns, H.C., Woodfine, R.G., 2013. Lithium isotope
900 evidence for enhanced weathering during Oceanic Anoxic Event 2. Nat. Geosci. 6,
901 668–672.
902 Pourmand, A., Dauphas, N., Ireland, T.J., 2012. A novel extraction chromatography and
903 MC-ICP-MS technique for rapid analysis of REE, Sc and Y: Revising CI-chondrite

and Post-Archean Australian Shale (PAAS) abundances. Chem. Geol. 291, 38–54.

Reijmer, J.J.G., 2021. Marine carbonate factories: Review and update. Sedimentology 68, 1729–1796.

Ruebsam, W., Mayer, B., Schwark, L., 2019. Cryosphere carbon dynamics control early Toarcian global warming and sea level evolution. Global. Planet. Change 172, 440–453.

Ruebsam, W., Reolid, M., Sabatino, N., Masetti, D., Schwark, L., 2020. Molecular paleothermometry of the early Toarcian climate perturbation. Global. Planet. Change 195, 103351.

Sabatino, N., Neri, R., Bellanca, A., Jenkyns, H.C., Baudin, F., Parisi, G., Masetti, D., 2009. Carbon-isotope records of the Early Jurassic (Toarcian) oceanic anoxic event from the Valdorbia (Umbria–Marche Apennines) and Monte Mangart (Julian Alps) sections: palaeoceanographic and stratigraphic implications. Sedimentology 56, 1307–1328.

Sabatino, N., Vlahović I., Jenkyns, H.C., Scopelliti, G., Neri, R., Prtoljan, B., Velic, I., 2013. Carbon-isotope record and palaeoenvironmental changes during the early Toarcian oceanic anoxic event in shallow-marine carbonates of the Adriatic Carbonate Platform in Croatia. Geol. Mag. 150, 1085–1102.

Sciunnach, D., Garzanti, E., 2012. Subsidence history of the Tethys Himalaya. Earth-Sci. Rev. 111, 179–198.

Scotese, C., 2014. Atlas of Jurassic paleogeographic maps, PALEOMAP Atlas for ArcGIS, Volume 4, The Jurassic and Triassic, Maps 32–42. Mollweide Projection, PALEOMAP Project, Evanston, IL.

Storm, M.S., Hesselbo, S.P., Jenkyns, H.C., Ruhl, M., Ullmann, C.V., Xu, W., Leng, M.J.,

Riding, J.B., Gorbanenko, O., 2020. Orbital pacing and secular evolution of the Early Jurassic carbon cycle. Proc. Natl. Acad. Sci. USA 117, 3974–3982.

Suan, G., Mattioli, E., Pittet, B., Lecuyer, C., Sucheras-Marx, B., Duarte, L.V., Philippe, M., Reggiani, L., Martineau, F., 2010. Secular environmental precursors to Early Toarcian (Jurassic) extreme climate changes. Earth Planet. Sci. Lett. 290, 448–458.

Taylor, S., McLennan, S.,, 1985. The Continental Crust: Its Composition and Evolution. Oxford Blackwell, pp. 311.

Them II T.R., Gill, B.C., Caruthers, A.H., Gröcke, D.R., Tulsky, E.T., Martindale, R.C., Poulton, T.P., Smith, P.L, 2017a. High-resolution carbon isotope records of the Toarcian Oceanic Anoxic Event (Early Jurassic) from North America and implications for the global drivers of the Toarcian carbon cycle. Earth Planet. Sci. Lett. 459, 118–126.

Them, T.R., Gill, B.C., Selby, D., Gröcke, D.R., Friedman, R.M., Owens, J.D., 2017b. Evidence for rapid weathering response to climatic warming during the Toarcian Oceanic Anoxic Event. Sci. Rep. 7, 5003.

Them, T.R., Gill, B.C., Caruthers, A.H., Gerhardt, A.M., Gröcke, D.R., Lyons, T.W., Marroquín, S.M., Nielsen, S.G., Trabucho Alexandre, J.P., Owens, J.D., 2018. Thallium isotopes reveal protracted anoxia during the Toarcian (Early Jurassic) associated with volcanism, carbon burial, and mass extinction. Proc. Natl. Acad. Sci. 115, 6596–6601.

Tostevin, R., 2021. Cerium Anomalies and Paleoredox. (Elements in Geochemical Tracers in Earth Systems Science). Cambridge University Press, Cambridge.

Tostevin, R., Shields, G.A., Tarbuck, G.M., He, T., Clarkson, M.O., Wood, R.A., 2016a.

Effective use of cerium anomalies as a redox proxy in carbonate-dominated marine settings. Chem. Geol. 438, 146–162.

Tostevin, R., Wood, R.A., Shields, G.A., Poulton, S.W., Guilbaud, R., Bowyer, F., Penny, A.M., He, T., Curtis, A., Hoffmann, K.H., Clarkson, M.O., 2016b. Low-oxygen waters limited habitable space for early animals. Nat. Commun. 7, 12818.

Trecalli, A., Spangenberg, J., Adatte, T., Follmi, K.B., Parente, M., 2012. Carbonate platform evidence of ocean acidification at the onset of the early Toarcian oceanic anoxic event. Earth Planet. Sci. Lett. 357, 214–225.

Ullmann, C.V., Hesselbo, S.P., Korte, C., 2013. Tectonic forcing of Early to Middle Jurassic seawater Sr/Ca. Geology 41, 1211–1214.

Webb, G.E., Kamber, B.S., 2000. Rare earth elements in Holocene reefal microbialites: a new shallow seawater proxy. Geochim. Cosmochim. Acta 64, 1557–1565.

Wilmsen, M., Neuweiler, F., 2008. Biosedimentology of the Early Jurassic post-extinction carbonate depositional system, central High Atlas rift basin, Morocco. Sedimentology 55, 773–807.

Woodfine, R.G., Jenkyns, H.C., Sarti, M., Baroncini, F., Violante, C., 2008. The response of two Tethyan carbonate platforms to the early Toarcian (Jurassic) oceanic anoxic event: environmental change and differential subsidence. Sedimentology 55, 1011–1028.

Xu, W., Ruhl, M., Jenkyns, H.C., Leng, M.J., Huggett, J.M., Minisini, D., Ullmann, C.V., Riding, J.B., Weijers, J.W., Storm, M.S., 2018. Evolution of the Toarcian (Early Jurassic) carbon-cycle and global climatic controls on local sedimentary processes (Cardigan Bay Basin, UK). Earth Planet. Sci. Lett. 484, 396–411.

973 Zhao, M.-Y., Zheng, Y.-F., 2014. Marine carbonate records of terrigenous input into
974 Paleotethyan seawater: Geochemical constraints from Carboniferous limestones.
975 Geochim. Cosmochim. Acta 141, 508–531.
976 Zhao, Y., Wei, W., Li, S., Yang, T., Zhang, R., Somerville, I., Santosh, M., Wei, H., Wu, J.,
977 Yang, J., Chen, W., Tang, Z., 2021. Rare earth element geochemistry of carbonates as
978 a proxy for deep-time environmental reconstruction. Palaeogeogr. Palaeoclimatol.
979 Palaeoecol. 574, 110443.
980 Zhao, Y., Wei, W., Santosh, M., Hu, J., Wei, H., Yang, J., Liu, S., Zhang, G., Yang, D., Li,
981 S., 2022. A review of retrieving pristine rare earth element signatures from carbonates.
982 Palaeogeogr. Palaeoclimatol. Palaeoecol. 586, 110765.

Fig. 1

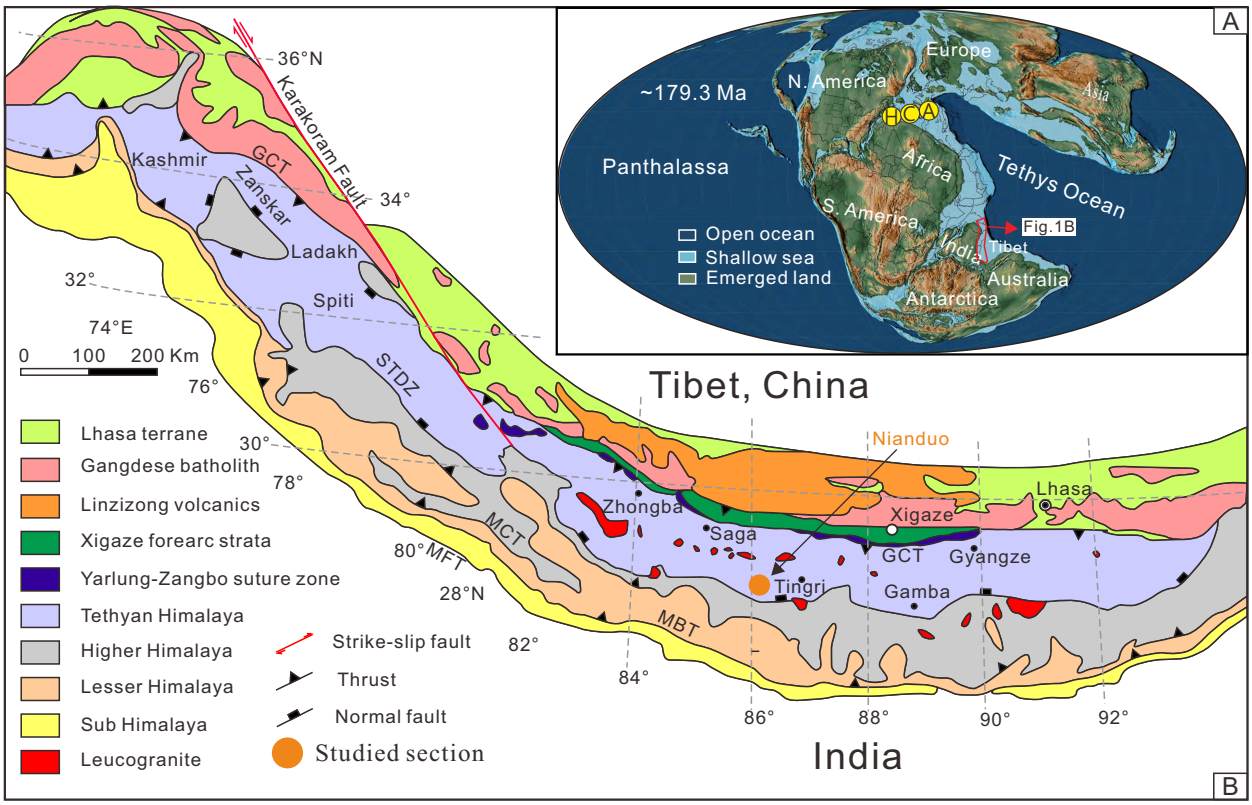
A
~179.3 Ma
Europe
N. America
Asia
Africa
Panthalassa
Tethys Ocean
S. America
India
Australia
Antarctica
Fig.1B
Tibet
Open ocean
Shallow sea
Emerged land
Tibet, China
36°N
34°
32°
74°E
0 100 200 Km
76°
78°
80°
82°
84°
86°
88°
90°
92°
30°
28°N
Karakoram Fault
GCT
Kashmir
Zanskar
Ladakh
Spiti
STDZ
MCT
MFT
MBT
Nianduo
Lhasa
Xigaze
Zhongba
Saga
GCT
Gyangze
Tingri
Gamba
India
Lhasa terrane
Gangdese batholith
Linzizong volcanics
Xigaze forearc strata
Yarlung-Zangbo suture zone
Tethyan Himalaya
Higher Himalaya
Lesser Himalaya
Sub Himalaya
Leucogranite
Strike-slip fault
Thrust
Normal fault
Studied section
B

Fig. 2

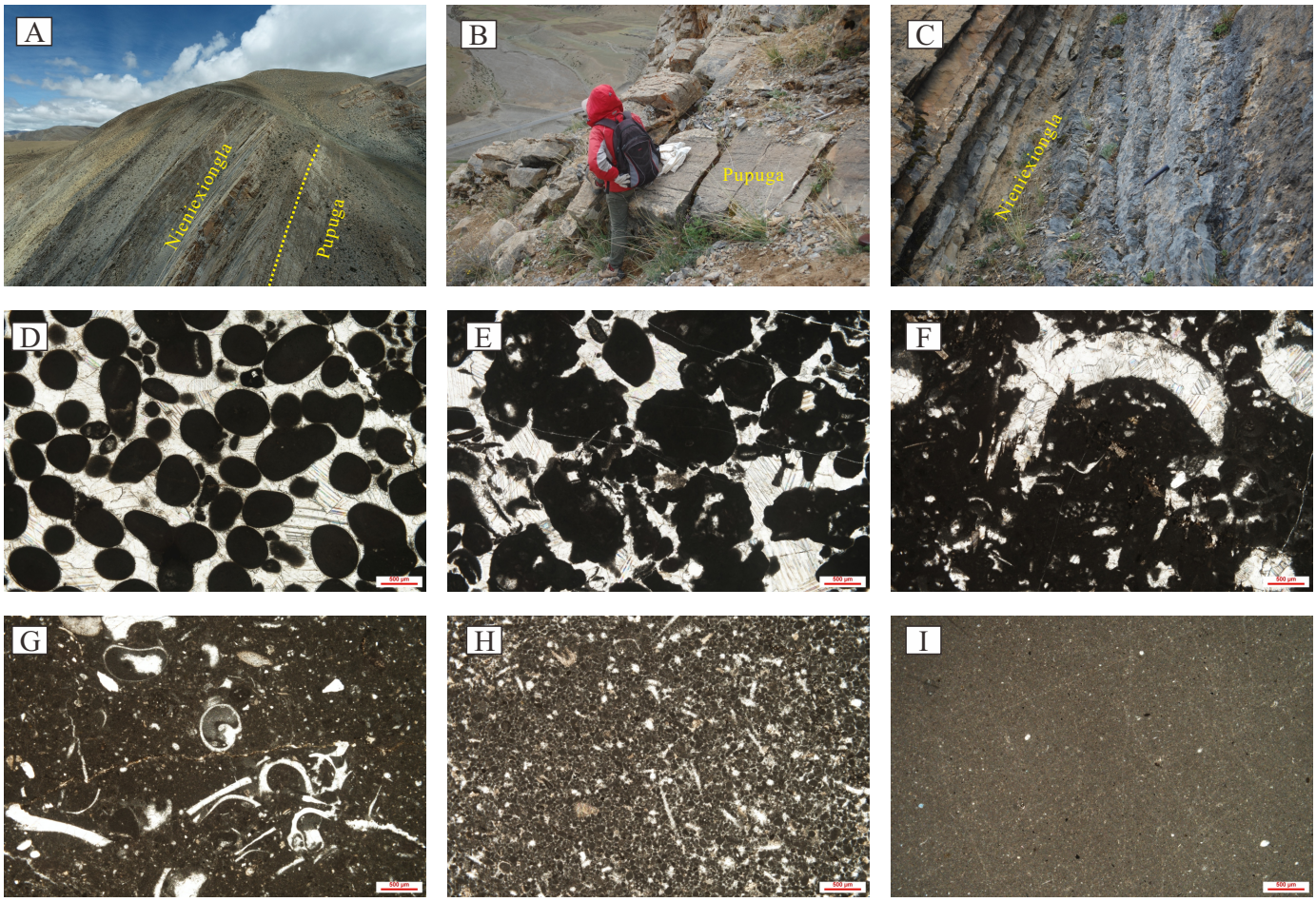

Fig. 3

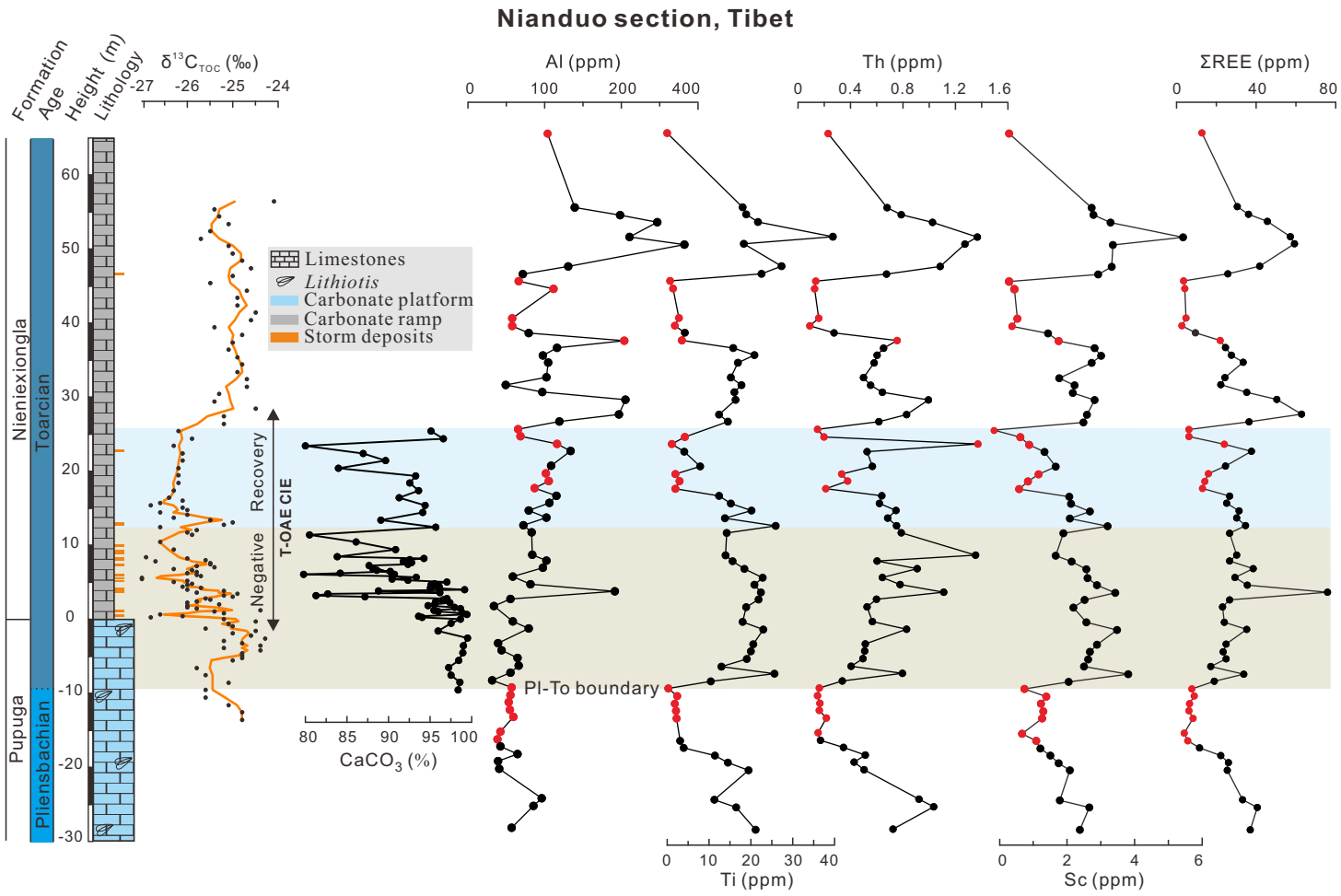
Nianduo section, Tibet
Formation
Age
Height (m)
Lithology
δ13CTOC (‰)
-27 -26 -25 -24
Al (ppm)
0 100 200 400
Th (ppm)
0 0.4 0.8 1.2 1.6
ΣREE (ppm)
0 40 80
Nieniexiongla
Pupuga
Toarcian
Pliensbachian
60 50 40 30 20 10 0 -10 -20 -30
Limestones
Lithiotis
Carbonate platform
Carbonate ramp
Storm deposits
Recovery
Negative
T-OAE CIE
Pl-To boundary
80 85 90 95 100
CaCO3 (%)
0 10 20 30 40
Ti (ppm)
0 2 4 6
Sc (ppm)

Fig. 4

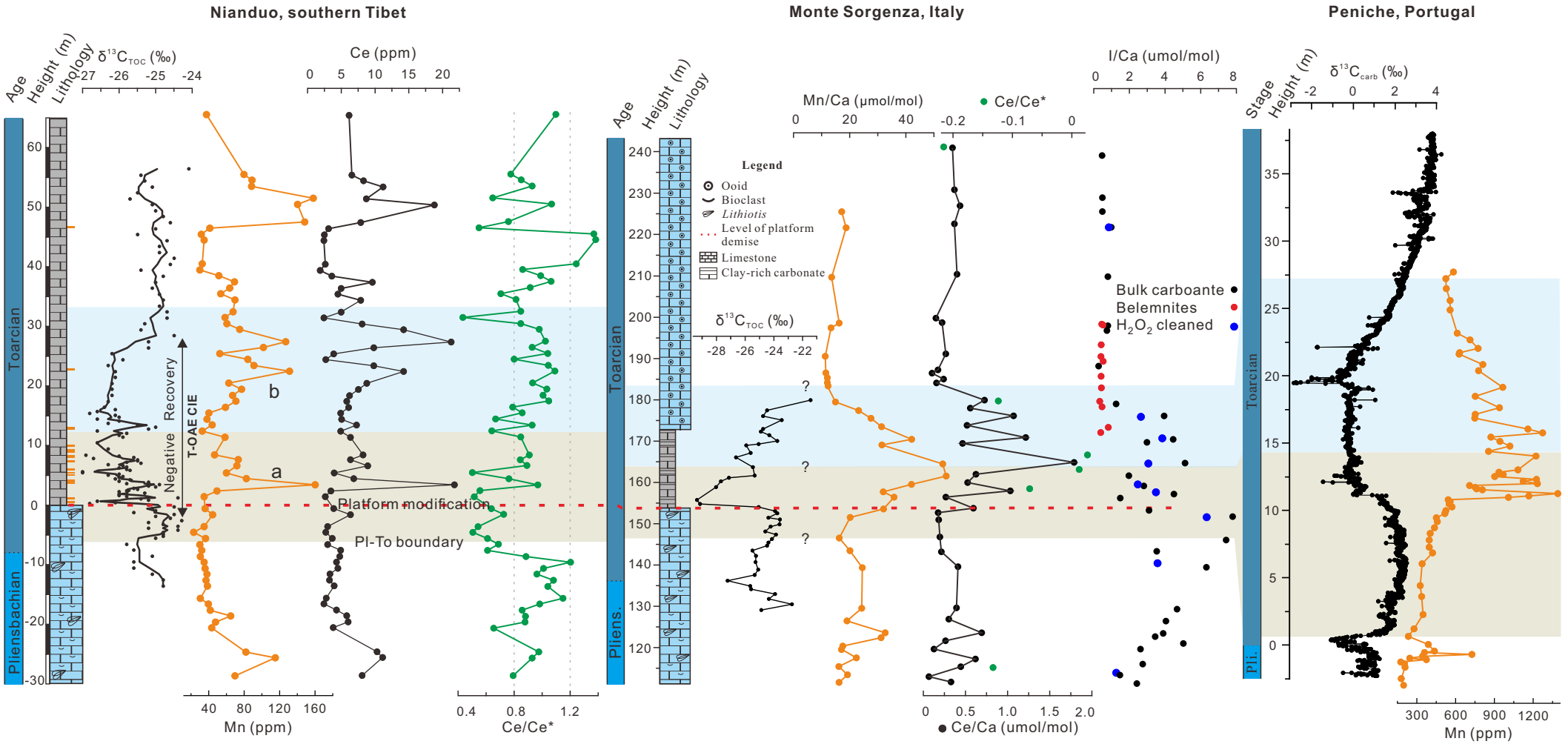
Nianduo, southern Tibet
Monte Sorgenza, Italy
Peniche, Portugal
Age
Height (m)
Lithology
δ13CTOC (‰)
Ce (ppm)
Mn (ppm)
Ce/Ce*
Mn/Ca (μmol/mol)
I/Ca (umol/mol)
δ13Ccarb (‰)
Stage
Toarcian
Pliensbachian
Pliens.
Pli.
Legend
Ooid
Bioclast
Lithiotis
Level of platform demise
Limestone
Clay-rich carbonate
Bulk carboante
Belemnites
H2O2 cleaned
Ce/Ca (umol/mol)
T-OAE CIE
Recovery
Negative
a
b
Platform modification
Pl-To boundary
?

Fig. 5

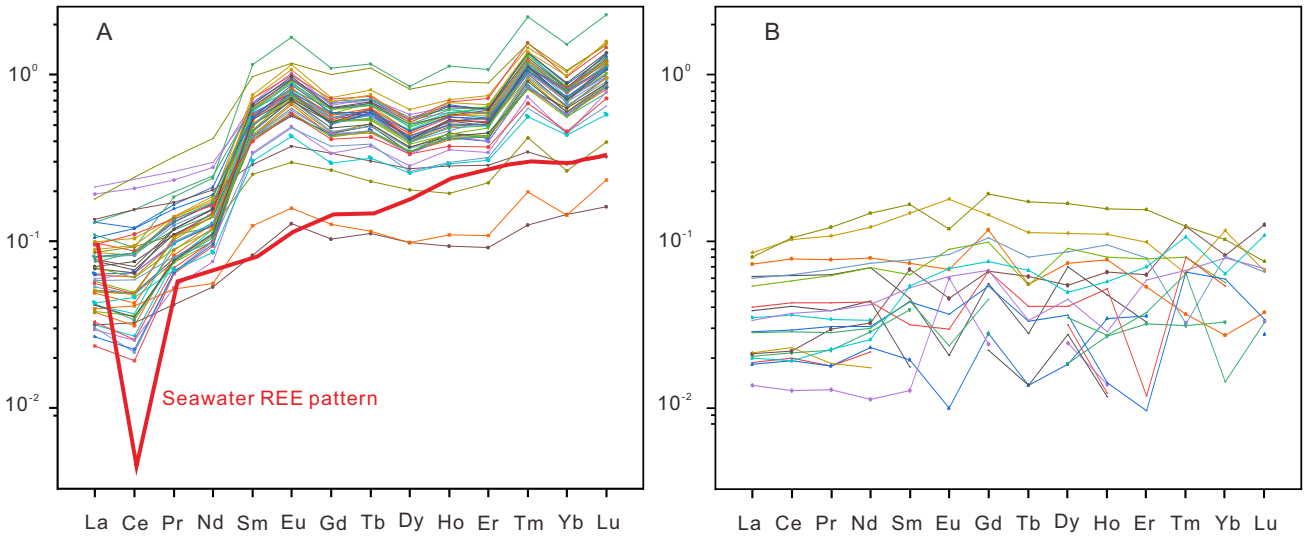
A
B
10^0
10^{-1}
10^{-2}
Seawater REE pattern
La Ce Pr Nd Sm Eu Gd Tb Dy Ho Er Tm Yb Lu

Fig. 6

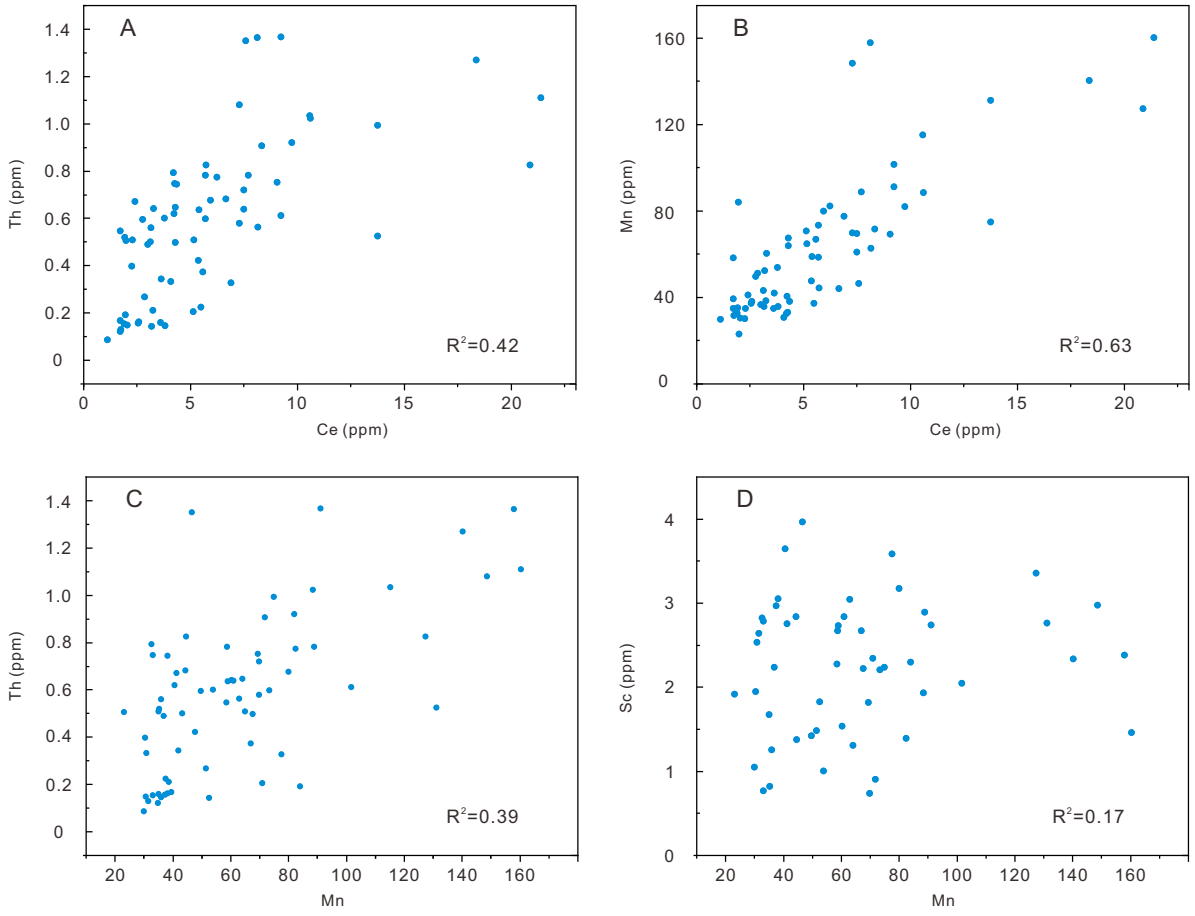
A
Th (ppm)
Ce (ppm)
R²=0.42
B
Mn (ppm)
Ce (ppm)
R²=0.63
C
Th (ppm)
Mn
R²=0.39
D
Sc (ppm)
Mn
R²=0.17

Fig. 7

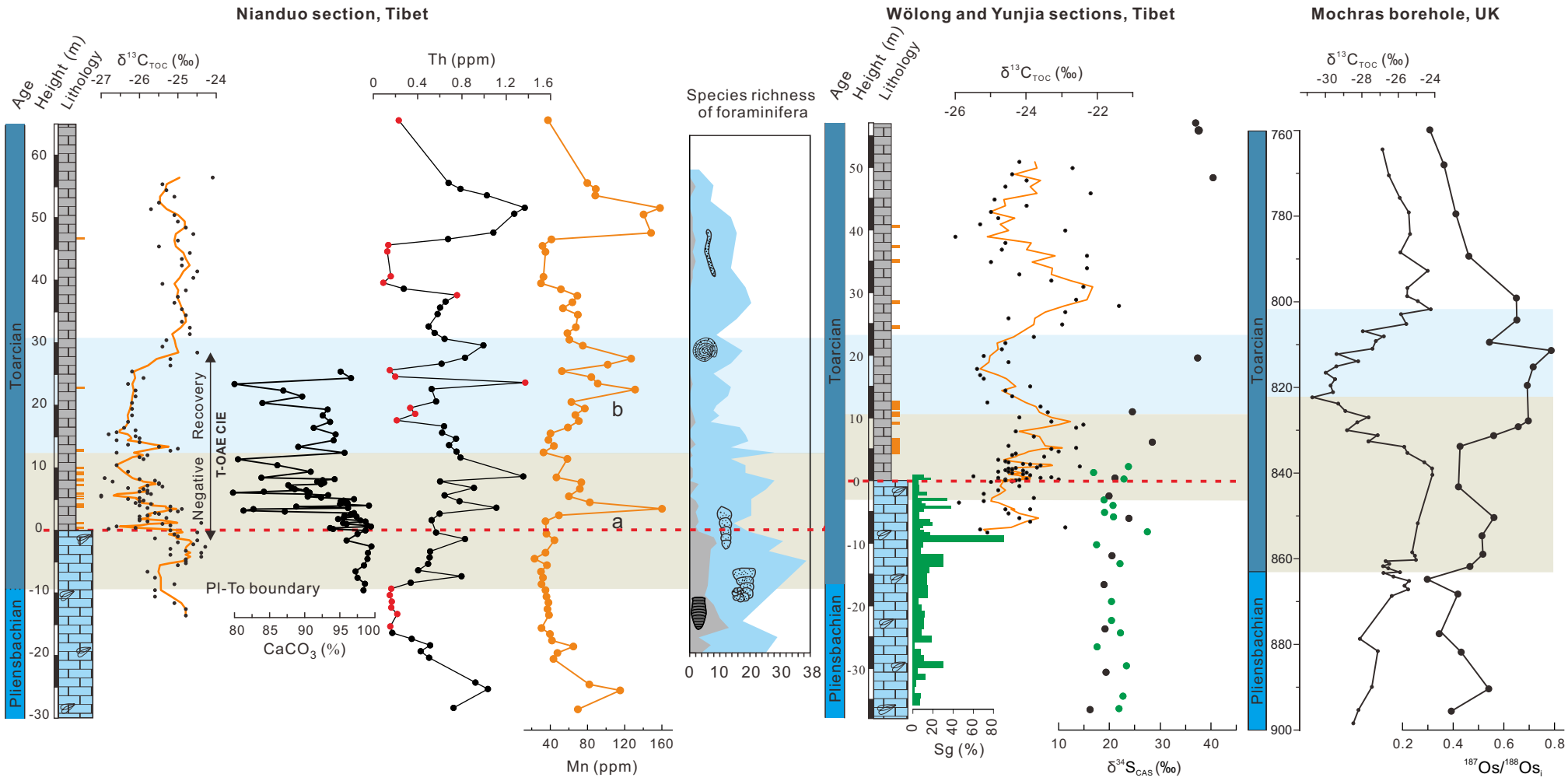
Nianduo section, Tibet
Age
Height (m)
Lithology
δ13CTOC (‰)
-27 -26 -25 -24
Th (ppm)
0 0.4 0.8 1.2 1.6
Species richness of foraminifera
Toarcian
Pliensbachian
60 50 40 30 20 10 0 -10 -20 -30
Recovery
Negative
T-OAE CIE
Pl-To boundary
80 85 90 95 100
CaCO3 (%)
40 80 120 160
Mn (ppm)
b
a
0 10 20 30 38
Wölong and Yunjia sections, Tibet
Age
Height (m)
Lithology
δ13CTOC (‰)
-26 -24 -22
50 40 30 20 10 0 -10 -20 -30
0 20 40 60 80
Sg (%)
10 20 30 40
δ34SCAS (‰)
Mochras borehole, UK
δ13CTOC (‰)
-30 -28 -26 -24
760 780 800 820 840 860 880 900
0.2 0.4 0.6 0.8
187Os/188Osi

Fig. 8

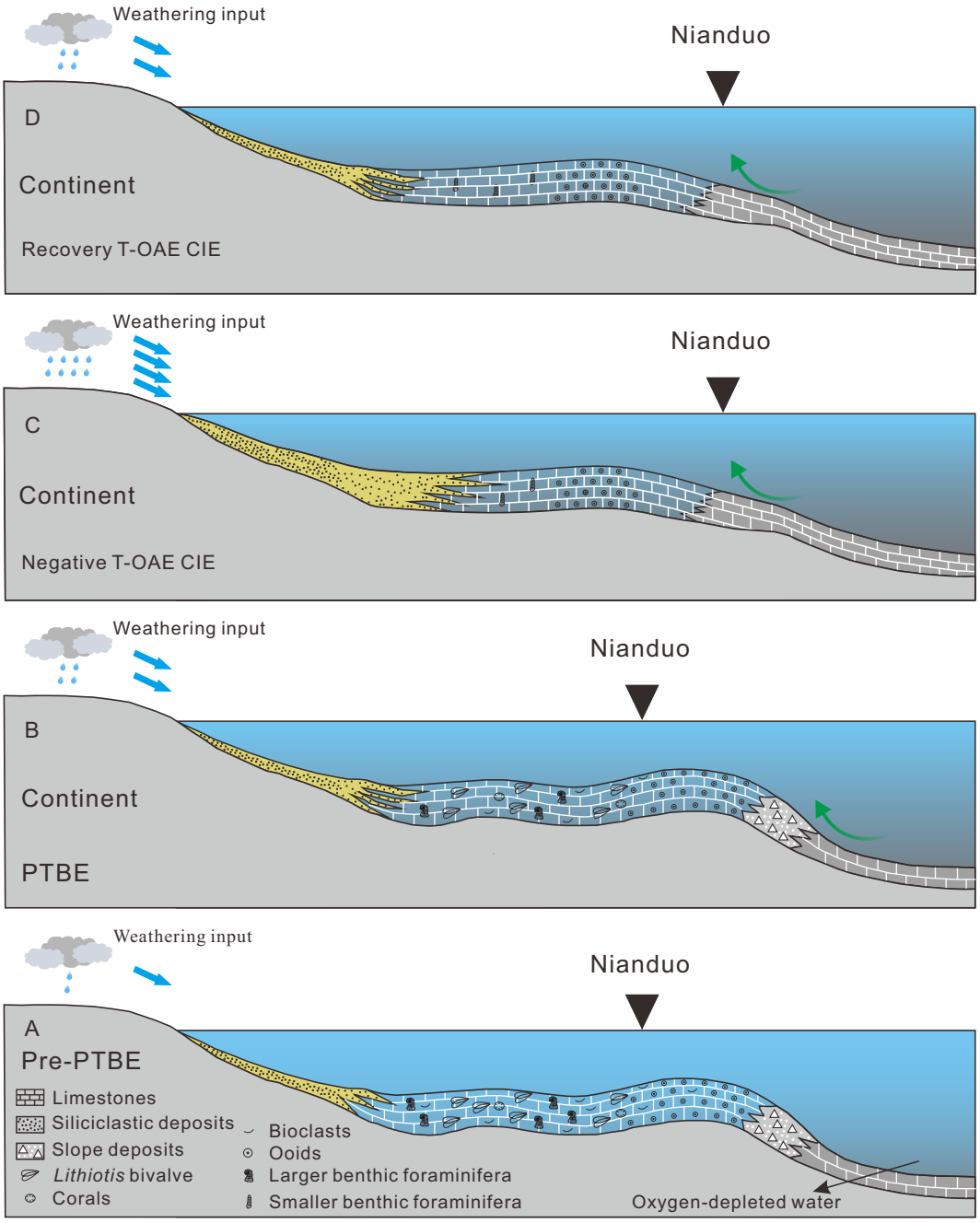
Weathering input
Nianduo
D
Continent
Recovery T-OAE CIE
Weathering input
Nianduo
C
Continent
Negative T-OAE CIE
Weathering input
Nianduo
B
Continent
PTBE
Weathering input
Nianduo
A
Pre-PTBE
Limestones
Siliciclastic deposits
Slope deposits
Lithiotis bivalve
Corals
Bioclasts
Ooids
Larger benthic foraminifera
Smaller benthic foraminifera
Oxygen-depleted water